Rapid source characterization of the Maule earthquake using Prompt Elasto-Gravity Signals

G. Arias[1], Q. Bletery[1], A. Licciardi[1], K. Juhel[1,2], J. P. Ampuero[1], and B. Rouet-Leduc[3]

[1]Université Côte d'Azur, IRD, CNRS, Observatoire de la Côte d'Azur, Géoazur, Sophia Antipolis, France
[2]Laboratoire de Planétologie et Géosciences - UMR 6112, Université de Nantes, CNRS, France
[3]Disaster Prevention Research Institute, Kyoto University, Kyoto, Japan

Key Points:

- A PEGS-based early warning algorithm for Chile
- Our algorithm could have estimated the magnitude of the Maule earthquake 90 s after origin time
- Deployment of seismic stations at optimal locations could greatly enhance the algorithm performance

Corresponding author: Gabriela Arias, arias@geoazur.unice.fr

Abstract

The recently identified Prompt Elasto-Gravity Signals (PEGS), generated by large earthquakes, propagate at the speed of light and are sensitive to the earthquake magnitude and focal mechanism. These characteristics make PEGS potentially very advantageous for earthquake and tsunami early warning. PEGS-based early warning does not suffer from the saturation of magnitude estimations problem that P-wave based early warning algorithms have, and could be faster than Global Navigation Satellite Systems (GNSS)-based systems while not requiring a priori assumptions on slip distribution. We use a deep learning model called PEGSNet to track the temporal evolution of the magnitude of the 2010 M_w 8.8 Maule, Chile earthquake. The model is a Convolutional Neural Network (CNN) trained on a database of synthetic PEGS – simulated for an exhaustive set of possible earthquakes distributed along the Chilean subduction zone – augmented with empirical noise. The approach is multi-station and leverages the information recorded by the seismic network to estimate as fast as possible the magnitude and location of an ongoing earthquake. Our results indicate that PEGSNet could have estimated that the magnitude of the Maule earthquake was above 8.7, 90 seconds after origin time. Our offline simulations using real data and noise recordings further support the instantaneous tracking of the source time function of the earthquake and show that deploying seismic stations in optimal locations could improve the performance of the algorithm.

Plain Language Summary

Tsunami early warning requires the fast and reliable estimation of an earthquake magnitude provided by the Earthquake Early Warning (EEW) systems. EEW systems are currently limited by the propagation speed of P-waves, which they rely on as natural information carriers. Even more problematic, EEW systems based on the first seismic arrivals tend to saturate with earthquake magnitude, and can become unreliable for magnitudes above 8. The recent discovery of Prompt Elasto-Gravity Signals (PEGS), which comprise gravitational changes generated by earthquakes, has raised hope to overcome these limitations because they travel at the speed of light, much faster than P-waves. We re-train the previously developed deep learning model PEGSNet to track the magnitude evolution of big earthquakes in the Chilean subduction zone from PEGS. Given the scarcity of big earthquakes, we simulate signals to train the model using synthetic sources and the seismic stations available in 2010 and 2021, augmented with empirical noise recorded by those stations. PEGSNet tracks the moment release 90 s after the origin time. PEGSNet's performance is limited by the seismic network configuration, the number of stations and noise level in the data. Deployment of seismic stations at optimal locations could greatly enhance early warning performance.

1 Introduction

Earthquakes redistribute Earth's mass, which produces changes in the gravitational field that lead to Prompt Elasto-Gravity Signals (PEGS) (Harms et al., 2015; Harms, 2016; Montagner et al., 2016; Heaton, 2017; Vallée et al., 2017). These signals precede conventional seismic waves and their amplitude depends on the earthquake source parameters, such as magnitude or focal mechanism (Vallée et al., 2017; Juhel et al., 2019; Vallée & Juhel, 2019; Zhang et al., 2020). These characteristics underlie the impact of their discovery and eventually their potential contribution to tsunami early warning (Juhel et al., 2018; Allen & Melgar, 2019; Shimoda et al., 2021; Licciardi et al., 2022; Zhang et al., 2022), since forecasting tsunami waves relies on the rapid estimation of earthquake magnitude (Melgar & Bock, 2013; Melgar et al., 2016; Setiyono et al., 2017) provided by Earthquake Early Warning (EEW) systems.

Conventional EEW systems have several limitations in estimating the final magnitude of an earthquake. Many EEW systems are designed to work with the first sec-

onds of P-waves to forecast quickly the magnitude and source information once an earthquake occurred (Allen & Kanamori, 2003; Wu & Zhao, 2006), but the onset does not contain enough information to predict how large an earthquake is going to be (Meier et al., 2016). Additionally, EEW algorithms use the data of accelerometers that record the very low-frequency displacements with low fidelity (Boore & Bommer, 2005; C. Ruhl et al., 2017). Overcoming these limitations is essential to prevent the underestimation of earthquake magnitude and impending hazards. For instance, during the 2011 Tohoku-Oki, Japan earthquake (M_w 9.0), the magnitude was estimated as M_w 8.1 at 116.8 s after the origin time (Hoshiba et al., 2011), which caused an underestimation of the subsequent tsunami amplitude (Hoshiba & Ozaki, 2014). Global Navigation Satellite Systems (GNSS) have been leveraged to overcome the drawbacks of earthquake and tsunami early warning (Bock & Melgar, 2016). GNSS-based algorithms can potentially solve the magnitude underestimation problem (Minson et al., 2014; C. Ruhl et al., 2017) but still use information (co-seismic ground deformation) travelling at the speed of P-waves (Minson et al., 2018; McGuire et al., 2021). GNSS-based algorithms that can accurately estimate the final rupture size also require the use of a priori constraints and inversion regularization that may be unpractical in real-time scenarios (McGuire et al., 2021).

PEGS present the fundamental property to propagate faster than seismic waves. In detail, they are the result of a direct gravity perturbation and an induced elastic response. The direct contribution consists of gravity perturbations ($\Delta\mathbf{g}$) caused by transient volumetric deformation and propagates at the speed of light; they arrive everywhere before any seismic wave. These gravity perturbations simultaneously act as secondary sources of elastic deformation in the whole Earth, inducing slight ground acceleration ($\ddot{\mathbf{u}}$). Due to the virtually instantaneous effect of the direct gravity perturbation, the induced ground acceleration also arrives before P-waves. The PEGS recorded by seismometers (acceleration $\mathbf{a}$) prior to the direct seismic wave arrival, is the sum of the direct gravity perturbation and the induced ground acceleration (Vallée et al., 2017):

$$\mathbf{a} = \Delta\mathbf{g} + \ddot{\mathbf{u}}. \tag{1}$$

In practice, $\Delta\mathbf{g}$ and $\ddot{\mathbf{u}}$ have opposite directions and similar magnitude, weakening the signal $\mathbf{a}$ (Heaton, 2017; Vallée et al., 2017).

The amplitudes of PEGS grow with the magnitude of the earthquake and depends on how fast the seismic moment rises (Vallée et al., 2017; Vallée & Juhel, 2019). Thus, it is unlikely to observe PEGS if the earthquake has low magnitude or if it ruptures slowly. For this reason, PEGS have only been identified for a handful of events (Vallée & Juhel, 2019). Though PEGS have shown strong potential to overcome the drawbacks of EEW systems, their extremely weak amplitudes (in the order of a few nanometers per second squared) have prevented operational applications. In this context, Licciardi et al. (2022) designed a deep convolutional neural network (CNN) called PEGSNet, to estimate earthquake location and to track the temporal evolution of the magnitude $M_w(t)$ of large earthquakes in Japan based solely on PEGS. The CNN is trained on a database made of synthetic PEGS waveforms plus real noise. Motivated by the success of PEGSNet in estimating the magnitude of the 2011 M_w 9.0 Tohoku-Oki earthquake in real time (Licciardi et al., 2022), we test here the portability of this algorithm to another region prone to mega-earthquakes: Chile. We first re-train PEGSNet on the seismic network that recorded the 2010 M_w 8.8 Maule earthquake in order to assess its performance in rapidly estimating the magnitude of this mega-earthquake. We then re-train the algorithm on the seismic network presently available in order to assess how PEGSNet would perform currently for an earthquake in Chile.

2 Data

Given the limited number of PEGS observations, we create a synthetic database to train the CNN. We compute the theoretical waveforms at the location of the avail-

able stations generated by 500,000 sources with different locations, source time functions, seismic moments and focal mechanisms. The waveform computation uses a pre-constructed moment tensor database, which uses normal mode theory to build Green's functions between sources and receivers (Juhel et al., 2019). To make the synthetic signals realistic, we then add empirical noise (i.e. actual noise recorded at each station) to the modeled waveforms.

We use two seismic networks that were functional during 11 months in two different time periods: 2009-2010 and 2021-2022, referred to hereafter as the 2010 network and the 2021 network, respectively. The 2010 network is composed of 21 stations selected from those available through IRIS in Chile, Argentina and Brazil. These seismic stations recorded the 2010 Maule earthquake, allowing us to test PEGSNet on data from the earthquake. The 2021 network contains 33 stations available via IRIS in Chile and Argentina. While there was no big earthquake between 2021 and 2022, we can evaluate on synthetic waveforms how PEGSNet would perform with the 2021 network configuration. The setup of the stations and synthetic sources is displayed in Figure 1.

For both networks, we select stations within a 2,000 km radius from all synthetic epicentres. According to Juhel et al. (2019), stations located in the P-wave extensional direction of the radiation pattern record strong gravity perturbation when deployed at distances between $1,000$ and $2,000$ km away from the epicentre of a large earthquake, due to the growing density anomaly generated by the rupture itself and the larger volume perturbed by the propagating seismic waves. At further distances, the perturbation decays, while at shorter distances the PEGS are rapidly hidden by the P-wave arrival.

2.1 Synthetics PEGS database

We compute synthetic PEGS following the method of Juhel et al. (2019). It requires as inputs the earthquake centroid location, station locations, focal mechanism, Source Time Function (STF) and seismic moment (M_0). We consider 994 source locations, equally spaced along the 20 km and 30 km iso-depths of the Chilean subduction megathrust, as shown in Figure 1. The longitude, latitude, depth, strike and dip angles of all sources are consistent with the Slab2.0 model (Hayes et al., 2018). Rake angles for each source are drawn from a normal distribution with mean 90° and standard deviation 10°, and magnitudes from a uniform distribution between 6.0 and 10.0. Moment is calculated as $M_0 = 10^{1.5M_w+9.1}$ (in Newton-meters). We draw the STF from the empirical model proposed by Meier et al. (2017):

$$STF(t) = M_0 \frac{f(t)}{\int f(t)\,dt}, \tag{2}$$

where

$$f(t) = t\exp\{-0.5(\lambda t)^2\}[1 + N(t)], \tag{3a}$$

$$\lambda = 10^{7.24-0.41\log(M_0)+\epsilon}, \tag{3b}$$

$$N(t) = 0.38\frac{n(t)}{\sigma}, \tag{3c}$$

The random variable ϵ accounts for variability in the STF duration for a given M_0 and is drawn from a Gaussian distribution with zero mean and standard deviation of 0.15. The random component $N(t)$ models the fluctuations observed in real STFs. $n(t)$ is the time integral of a Gaussian noise time series with zero mean and standard deviation σ. Examples of STFs for different magnitudes are plotted in Figure 2.

The resulting synthetics are three-component (Z, N and E) acceleration waveforms depicting the PEGS generated by earthquakes of large magnitude that might potentially occur in the Chilean subduction megathrust. They are sampled at 1 Hz and stored in windows of 700 s duration, centered at the origin time.

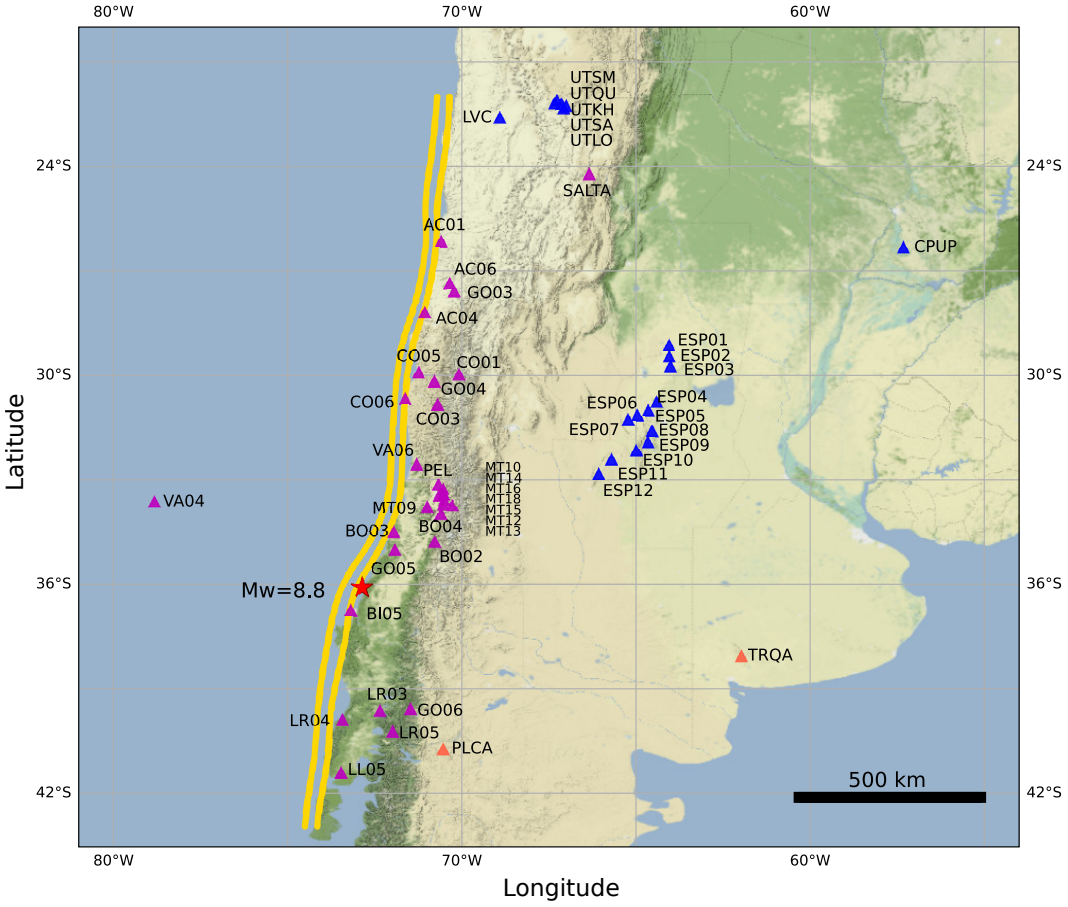

Figure 1. Two seismic networks and earthquake sources used in this work. The yellow dots indicate the location of the synthetic sources. Blue triangles represent the stations of the 2010 network, purple triangles those of the 2021 network, and orange triangles the stations that belong to both networks. The red star represents the 2010 M_w 8.8 Maule earthquake epicenter.

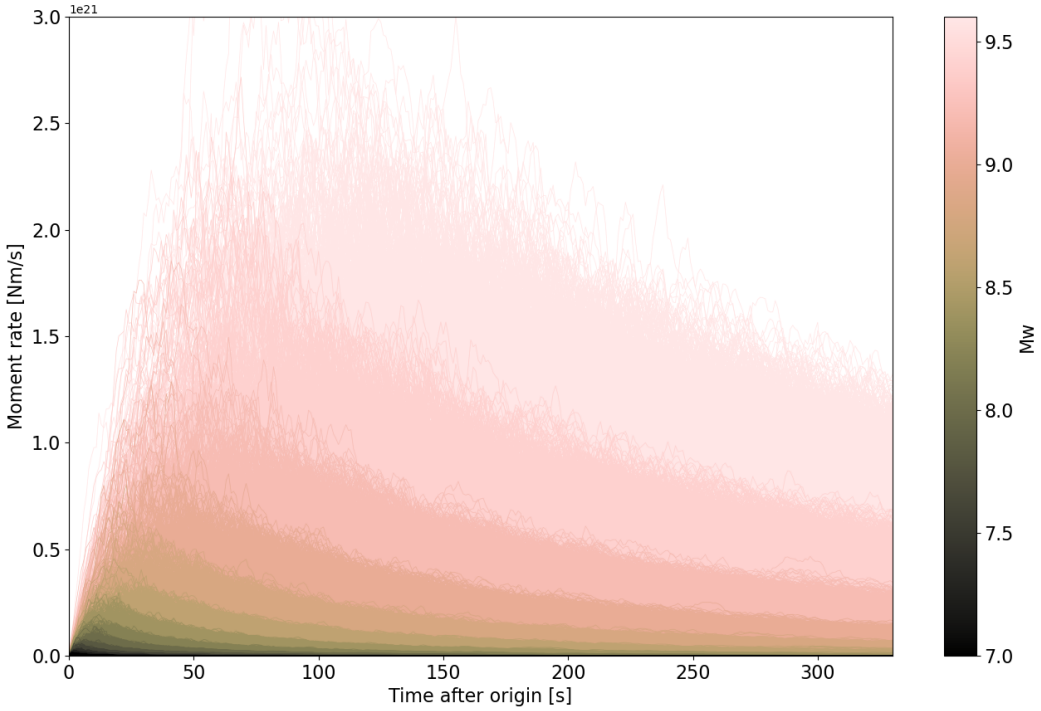

Figure 2. Source time functions used to generate the synthetic PEGS database, corresponding to magnitudes between 7.0 and 9.6.

2.2 Empirical noise database

For both configurations, 2010 and 2021, the noise database is extracted from 11 months of continuous recordings, from May 2009 to April 2010 and from February 2021 to January 2022, respectively. The database is composed of 1-hour long traces that we pre-process as follows: instrumental response, mean and linear trend removal, and decimation to 1 Hz. We filter the recordings and synthetic waveforms as indicated in Vallée et al. (2017), using a 2.0 mHz high-pass, Butterworth, 2 poles, causal filter and a 30.0 mHz low-pass, Butterworth, 6 poles, causal filter. Then, we extract data windows (mainly composed of noise) of 700 s from the 1-hour-long traces at randomly selected starting times.

Finally, we randomly add these noise samples to the synthetic PEGS and store each waveform as a 700 s long time series, centered on the earthquake origin time. We calculate the P-wave arrival time corresponding to each event-station pair in the synthetic waveform database, then set the signal to zero after the P-wave arrival time, to use only information contained in PEGS.

The database is divided into three parts: training, validation and test sets that comprise 80%, 10% and 10% of the database, respectively. As in Licciardi et al. (2022), we clip traces at ± 10 nm/s^2 to eliminate high amplitudes and to limit the influence of high levels of noise. We scale amplitudes by 10 nm/s^2 to facilitate the convergence of the optimizer and to preserve information on the relative amplitudes of the PEGS. Additionally, we set to zero the amplitudes of the traces of 5% of the stations, randomly selected, for each event to simulate missing data and to limit over-fitting.

3 PEGSNet

3.1 Architecture

PEGSNet is a CNN that combines convolutional layers and fully connected layers in sequence (Fig. 3), adopting a multi-station approach (Licciardi et al., 2022). We work with image-like inputs to train PEGSNet. Data are organised as images of size (M,N,c). M (= 315) is the number of samples in 315 s long trace time windows, N is the number of stations and c (= 3) is the number of components: vertical, east and north. The three outputs of the model are latitude (ϕ), longitude (λ) and moment magnitude ($M_w(t)$) at the time t of the last sample of the window.

The original architecture of PEGSNet designed by Licciardi et al. (2022) consists of eight convolutional blocks, but in this work, we use seven since the number of stations is less than that used in the cited work. Each block has one convolutional layer with rectified linear unit (ReLu) activation function and one dropout layer. Each convolutional layer has 32 filters from block 1 to block 4, 64 filters in blocks 5 and 6, 128 filters in block 7. Each convolutional layer uses a fixed kernel size of 3×3 and also a spatial dropout with a fixed rate of 4%. From block 4 we add maximum pooling layers to reduce the dimension of the input features by a factor of 4. This output is flattened and fed to a sequence of two dense layers of size 512 and 256, with a ReLu activation function and a spatial dropout with a rate of 4%. The output layer consists of three neurons that perform regression through a hyperbolic tangent activation function (Figure 3 **a**). The number of parameters in the network is 1,535,139.

3.2 Training and testing

The labeled ϕ and λ correspond to the true values used for the computation of the synthetic PEGS of each event. The labeled $M_w(t)$ is the moment magnitude used to calculate the synthetic PEGS at the time of the last waveform sample t. We extract the data of a determined running time window that starts at a random time t_1 and has a length of 315 s. Then, we assign the value of $M_w(t_1 + 315s)$ as the corresponding label (Fig. 3 **b** and **c**). In other words, PEGSNet is given a 315s snapshot of the network's seismograms, and has to output the magnitude at the end of this snapshot. The loss between the ground truth and the predicted values is minimized during training (200 epochs and batches of size 512) by measuring the mean absolute error. At the end of each epoch, the model is evaluated on the validation set. The model whose loss value is the lowest on the validation set is selected as the final model and is evaluated once again on the test set. We train PEGSNet twice: once on the 2010 and once on the 2021 networks.

The process of testing is as follows: for each sample in the test set, a 315 s-long window $[t_1, t_2 = t_1 + 315s]$ slides through the data with a time step of 1 s. The starting window ends at the earthquake origin time t_0 ($t_2 = t_0$ and $t_1 = t_0 - 315s$) and the final window starts at the earthquake origin time ($t_2 = t_0 + 315s$ and $t_1 = t_0$). In between, PEGSNet reconstructs the STF by predicting $M_w(t_2)$ at each time step of 1 s.

4 PEGSNet performance in Chile in 2010

4.1 Overall performance

PEGSNet estimates the latitude ϕ and longitude λ of synthetic earthquakes, with errors on the order of 0.5° [55 km] for latitude and 0.2° [22 km] for longitude, after 120 sec (see supplementary material Fig. S1). These results should not be over-interpreted since we implicitly provide the P-wave arrival times to PEGSNet by setting waveforms to 0 after the P arrival, making the location problem relatively trivial. We therefore mainly focus our analysis on the magnitude estimation.

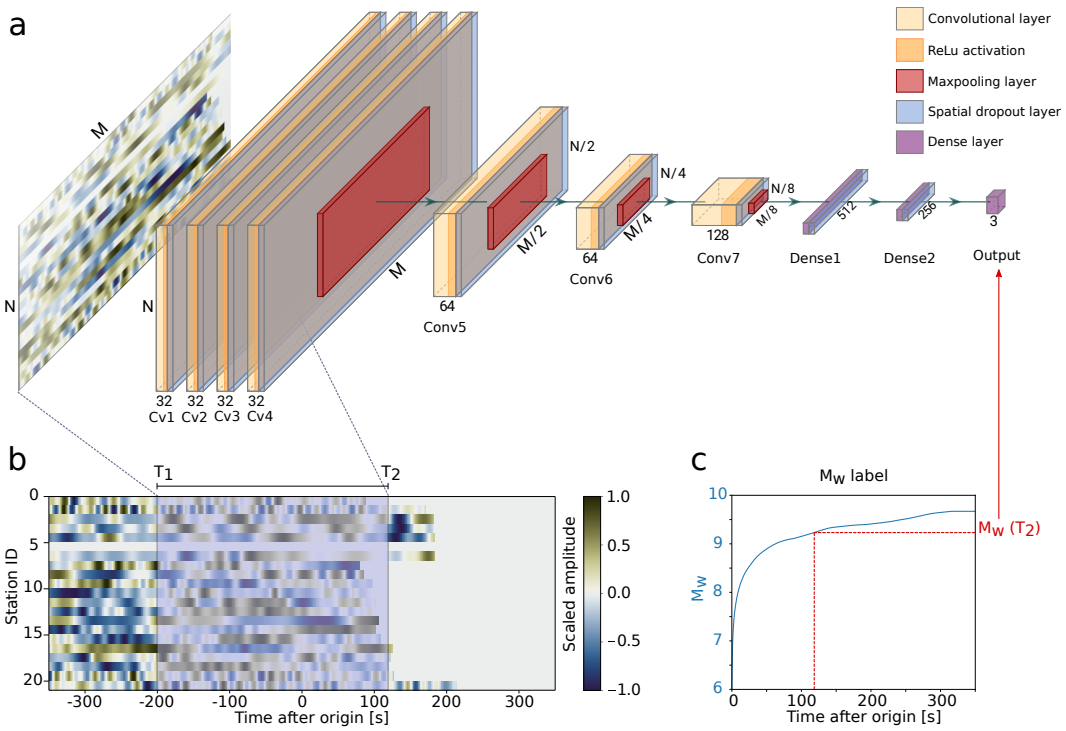

Figure 3. **a** PEGSNet architecture: The input data is a three-channel image (each channel corresponds to each component Z, N and E), of shape MxN, where M is the number of samples and N the number of seismic stations. **b** One example of the input data from the training database (vertical component only). The shaded area represents the input data for PEGSNet. The beginning of the input window T_1 is randomly selected and $T_2 = T_1 + 315$ s. **c** The blue line corresponds to the moment $M_w(t)$ for the selected event. The label assigned is $M_w(T_2)$ at the end of the window.

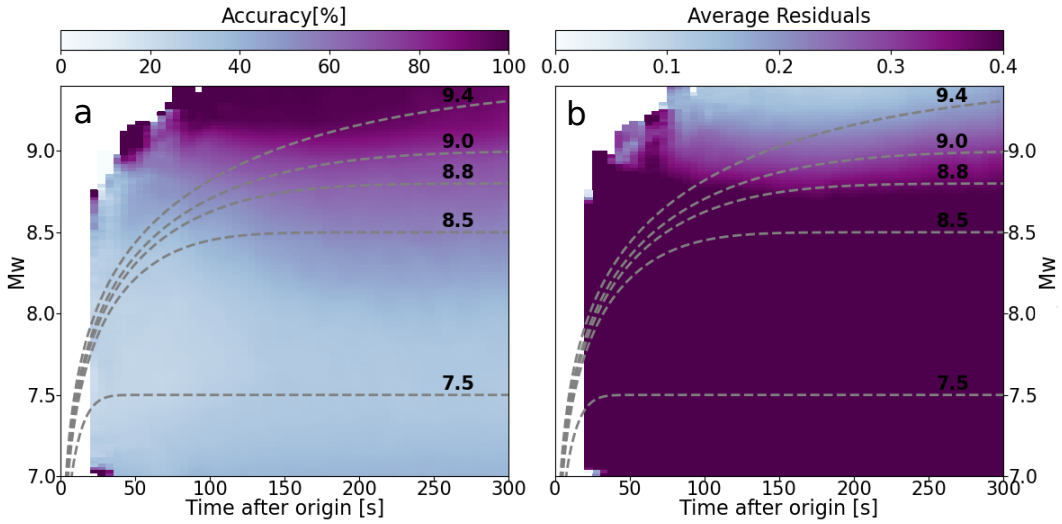

Figure 4. **a** Accuracy of the predictions on the test set as a function of time and magnitude. In each bin (pixel), the color represents the number of predictions whose distance to the ground truth is less than 0.4 magnitude units, divided by the total number of samples in the bin. The dashed lines represent the average values of the true $M_w(t)$ for events with the final magnitude indicated by the corresponding number. **b** Density map of the average residuals between the true and predicted magnitudes as a function of time and magnitude.

We simulate a real-time scenario on each sample of the test set, by analyzing the data with a running time window of 315 s. Each window is fed to PEGSNet which estimates $M_w(t)$, the magnitude at the time of the last sample of the time window. Then, the window is shifted in steps of 1 s as PEGSNet progressively reconstructs the STF. We can evaluate how reliable the results are through accuracy maps (Fig. 4). We define accuracy as the number of successful predictions divided by the total number of samples, with a prediction considered successful when its difference with the ground truth is less than 0.4 magnitude units. The maps in Fig. 4 are calculated using all the samples of the test set. The outcome indicates that the model can track the moment released by earthquakes with magnitude equal to or higher than 8.8 with accuracy above 60% (Fig. 4**a**) and errors below 0.37 (Fig. 4**b**), starting at 100 s after origin time. Earthquakes of magnitudes between 8.2 and 8.7 can be estimated with accuracy between 33% and 54% and errors above 0.42, 100 s after origin time.

4.2 Performance on Mw 8.8 earthquakes

We test PEGSNet's performance on M_w 8.8 synthetic earthquakes distributed everywhere along the Chilean subduction fault. Figure 5**a** shows the probability density of the magnitude estimation on the test set for all the predictions of events with final magnitude $M_w = 8.8 \pm 0.5$. Following the red solid line, which is the mode of the predictions, we see a clear underestimation of the magnitude before 100 s (when the true M_w is generally below 8.7 in our STF database) followed by a sudden jump after which the model starts tracking the evolution of the magnitude. This indicates that PEGSNet does not detect PEGS when the earthquake magnitude is below 8.7 and that estimations below that magnitude threshold should be interpreted as an absence of detected signal. Above this value, estimations start to be reliable, indicating the ongoing occurrence of a very large ($M_w \geq 8.7$), likely tsunamigenic, earthquake.

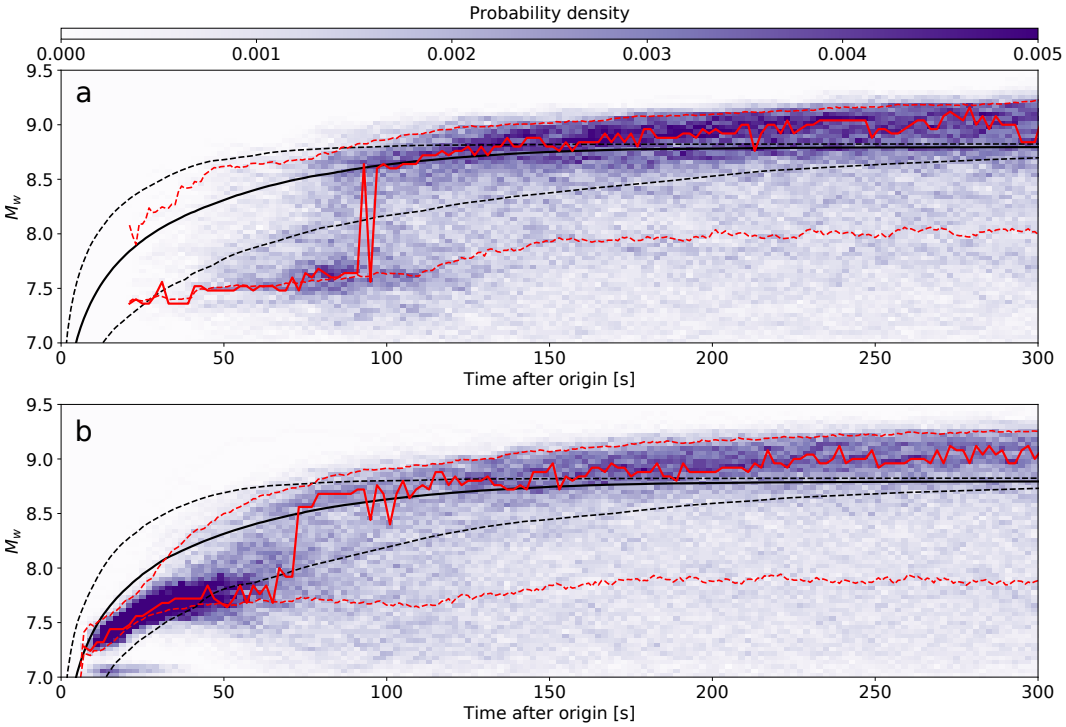

Figure 5. **a** Probability density of the magnitude estimation on M_w 8.8 synthetic earthquakes distributed everywhere along the Chilean subduction fault, with the 2010 network. The solid red line is the mode of the distribution. The red dashed lines limit the range between the 95 and 25 interquartiles. The solid black line is the median of the ground truth, and the dashed black lines limit the range between the 95 and 5 interquartiles. **b** Same as **a** for the 2021 network.

4.3 Playback of the Maule Earthquake

In order to validate the performance of PEGSNet, we use the actual Maule earthquake recordings. The processing of the raw data is the same as the one described in the Data section. We feed the model with the processed signals. The model outputs magnitude estimations every second starting at the origin time of the earthquake and using the previous 315 s of data, as described in the PEGSNet architecture section. We compare the results to the STF extracted from the SCARDEC database (Vallée & Douet, 2016) (Fig. 6). We observe a clear underestimation of the earthquake magnitude in the first 90 s. After 90 s, the model starts approaching the correct magnitude evolution.

We also compare our result to estimations obtained by other early warning algorithms such as G-larmS (C. J. Ruhl et al., 2019) and M-LARGE (Lin et al., 2021). The G-larmS estimation of the STF approaches the real STF before PEGSNet's (Fig. 6). This belated stabilization is mainly due to the small number of stations available for PEGSNet. The same model trained with data recorded by a higher number of stations can give better results, as seen in the Tohoku earthquake case (Licciardi et al., 2022). G-larmS is coupled to the seismic point-source algorithm of ShakeAlert (C. Ruhl et al., 2017; C. J. Ruhl et al., 2019), which is an EEW system that uses a combination of the amplitude and frequency content of the first seconds of the P-wave arrival to estimate source parameters (C. Ruhl et al., 2017). Therefore, G-LarmS relies on prior constraints. M-LARGE is a deep learning model that characterizes earthquake magnitude in real time using data from more than 120 stations of the Chilean HR-GNSS network (Lin et al., 2021). M-LARGE takes 40 s to reach values within a range of 8.8±0.3. However, at that time the earth-

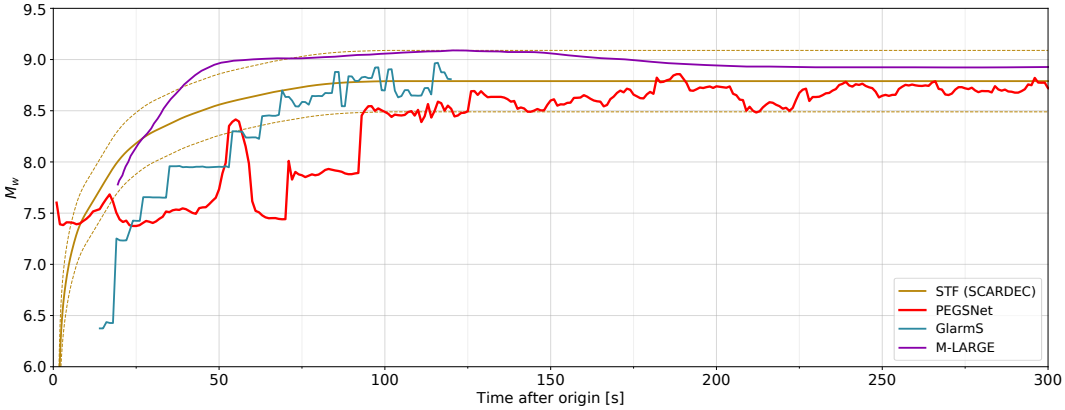

Figure 6. PEGSNet performance on real data for the Maule earthquake. The red curve shows the magnitude estimated by PEGSNet as a function of time using the recordings of the Maule earthquake. It is compared to the STF of the Maule earthquake in the SCARDEC database (Vallée & Douet, 2016) and to the estimations obtained by the G-larmS and M-LARGE algorithms. The golden dashed lines indicate ±0.3 magnitude units around the SCARDEC STF.

quake is still ongoing and the final magnitude value is not yet reached (see the golden curve in Fig. 6). For both G-larmS and M-LARGE, the results rely on using a priori assumptions on the slip distribution (McGuire et al., 2021) and are in contradiction with statistical analysis of earthquake source time functions (Meier et al., 2017). On the contrary, our approach requires no such a priori constraints and achieves similar theoretical performance only by leveraging signals travelling faster than seismic waves.

We perform two additional tests to assess the reliability of the model. In the first test, we generate synthetic PEGS using the SCARDEC STF of the Maule earthquake (Vallée & Douet, 2016) and add 1,000 different windows of noise recordings randomly taken from the test set. We then feed the model with these waveforms. The estimations indicate an accurate magnitude estimation starting a little after 100 s (Fig. 7). The second test consists in feeding the model with the 1,000 windows of noise, to check that the estimations of M_w do not exceed 8.7, which is the sensitivity level of PEGSNet (Fig. 8). The median of the magnitude estimations tends to remain constant at around 7.2, this value is considered the baseline corresponding to no PEGS detection.

5 PEGSNet performance in Chile in 2021

5.1 Overall performance

The results on the synthetic test set for the location, ϕ and λ, with the 2021 network are displayed in the supporting information (Fig. S2). The estimations of latitudes have errors up to 0.37° (41 km) and the ones of longitudes present up to 0.1° (11 km), 90 s after the origin. These location results are better than with the 2010 network. This is because the estimations rely on the P-wave arrival times and the present network contains more stations closer to the earthquake source.

According to the accuracy calculations, PEGSNet on the 2021 network can track the moment released by earthquakes with magnitude equal to or higher than 8.8 with an accuracy above 55% (Fig. 9 **a**) and errors below 0.46 (Fig. 9 **b**), 100 s after the origin time. For earthquakes with magnitude between 8.2 and 8.7, the accuracy goes from 30% to 47% and errors between 0.5 and 0.75, after 100 s from the origin time. We select this time value in order to compare with the results obtained for the 2010 network,

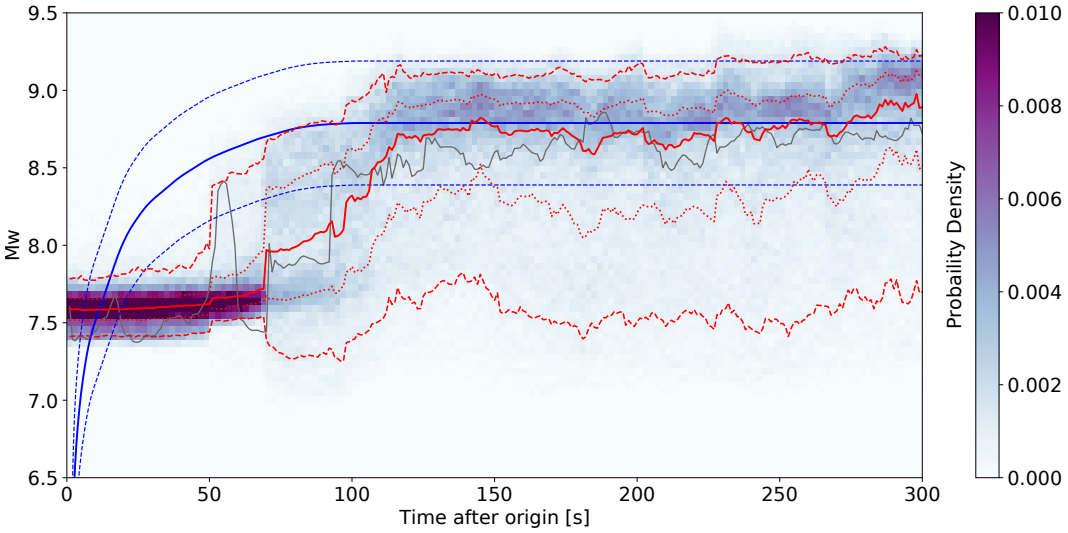

Figure 7. Density plot of PEGSNet magnitude estimations from 1,000 synthetic signals made of synthetic PEGS corresponding to the Maule earthquake source, augmented with 1,000 random noise time windows. The blue solid line represents the true STF taken from the SCARDEC database (Vallée & Douet, 2016), the same that we used to model the synthetics. The dashed blue lines indicate ±0.4 magnitude units around the SCARDEC STF. The red solid line is the median of the obtained distribution, the dotted red lines are the Q1-Q3 interquartile range and the dashed red lines limit the 5th and 95th percentiles. The gray solid line represents the magnitude estimated by PEGSNet using real data (same as in Fig. 6).

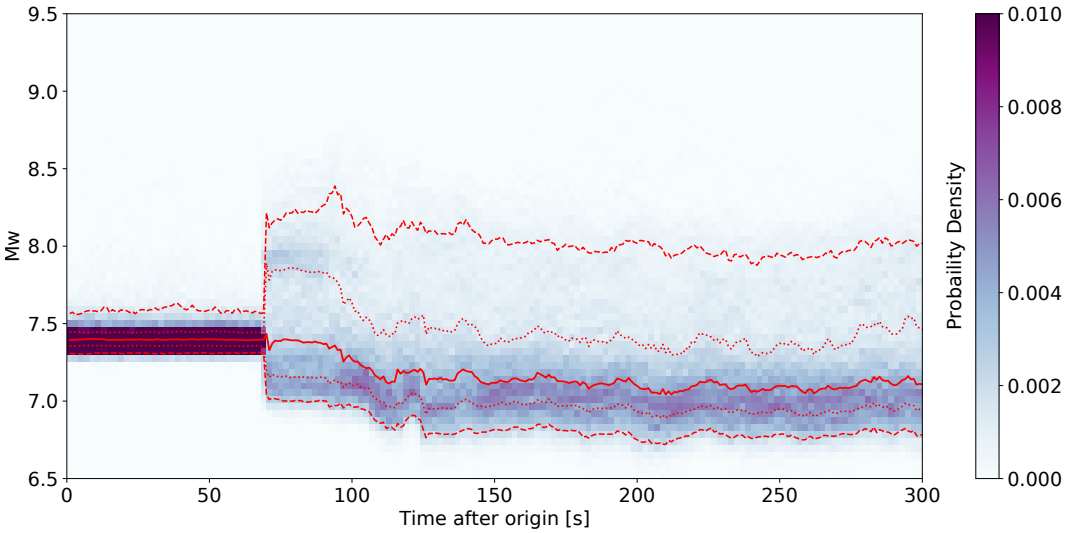

Figure 8. Magnitude estimations obtained by applying PEGSNet to noise: same as Fig. 7 but removing the synthetic PEGS from the input data.

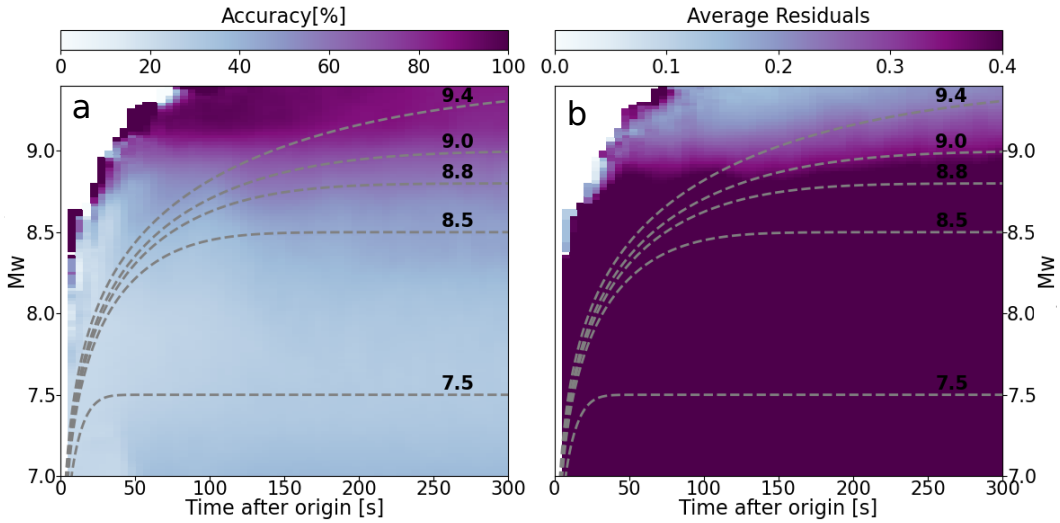

Figure 9. Same as Fig. 4 for the 2021 network.

which are better than in the present configuration. The reason is that the 2021 network is mainly parallel and close to the sources, where the expected PEGS amplitudes of subduction earthquakes are minimal (Fig. 10) (Vallée & Juhel, 2019). The leading contribution to the results is given by the only station located far from the trench, TRQA.

This highlights that PEGSNet performance is not only sensitive to the number of stations but also to their spatial distribution. According to the results obtained, PEGSNet's performance is more favorable with the contribution of stations located in the eastern part of the continent and far away from the sources, that is to say, in Argentina. For earthquakes comparable in magnitude to the Maule event, the ideal observation location for PEGS is ≈ 800 to 1,500 km west of the source (Fig. 10). With potential sources distributed all along the Andean subduction fault, this defines a geographical band on where deploying stations could dramatically benefit PEGS-based tsunami warning systems.

5.2 Performance on Mw 8.8 earthquakes

The probability density of the magnitude estimation on the test set for all the estimations of events with final magnitude $M_w = 8.8 \pm 0.5$ are shown in Figure 5 **b**. Following the mode (red solid line), we see that we also underestimate the magnitude, but this time until 70 s approximately, followed by a jump after which the model starts tracking the evolution of the magnitude. This faster estimation compared to the 2010 case is because, in the 2021 scenario, there are more stations that are deployed close to the synthetic sources. This indicates that with the present seismic network, PEGSNet would output a faster magnitude estimation for a magnitude 8.8 event than with the seismic network available in 2010. However, for slightly smaller events ($8.5 < M_w < 8.8$), PEGSNet would perform better on the seismic network of 2010 than on the present one.

6 Discussion

6.1 Noise analysis

To evaluate the influence of the noise amplitude on PEGSNet's performance, we calculate the accuracy using different groups of samples of the test set, divided according to the noise level. We compute the standard deviation of a five-minute window of

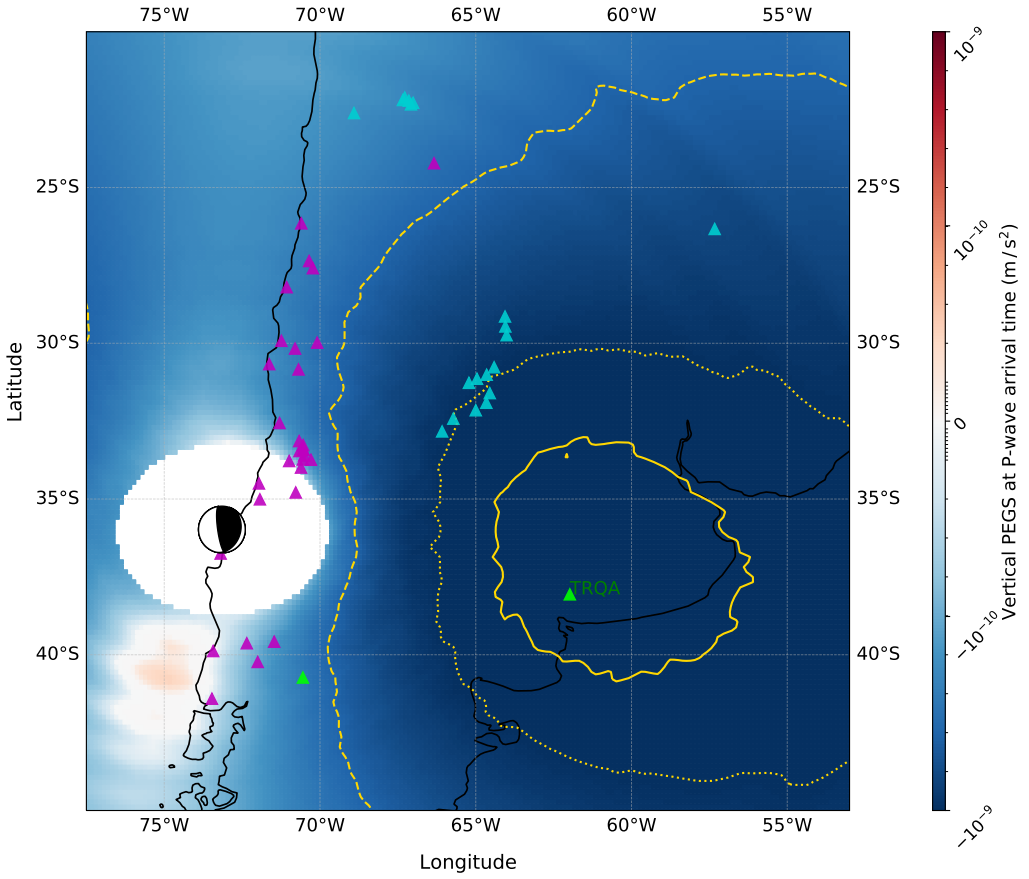

Figure 10. Spatial distribution of the maximum PEGS amplitude for the Maule earthquake, in the vertical component (at the P-wave arrival time). Turquoise and fuchsia triangles represent stations of the 2010 and 2021 networks, respectively. Green triangles are the stations common to the two networks

data before the P-wave arrival for each sample of the test set, and subsequently the median of the standard deviation over the whole seismic network. For both the 2010 and 2021 seismic networks, we then divide the test sets into 4 subsets defined by the three quartiles of the distribution: Q1, Q2 and Q3. The values of the three quartiles are displayed in Figs. 11**a** and 12**a** for the 2010 and 2021 networks , respectively. In both cases, the accuracy of the estimations decreases when the level of noise increases. This is summarized in Table 1, where the accuracy values have been calculated for the events with magnitude equal to or higher than 8.8, after 100 s of the origin time. Even though the level of noise of the 2010 network is higher than the one of the 2021 network, the accuracy of the estimations is better. These results come from the fact that 2010 network contains stations where the amplitudes of PEGS are large, while 2021 network stations are very close to the sources and the amplitudes of PEGS are small (Fig. 10). Thus, in our case study, the spatial configuration of the seismic network is more important than the number of stations and even than its level of noise.

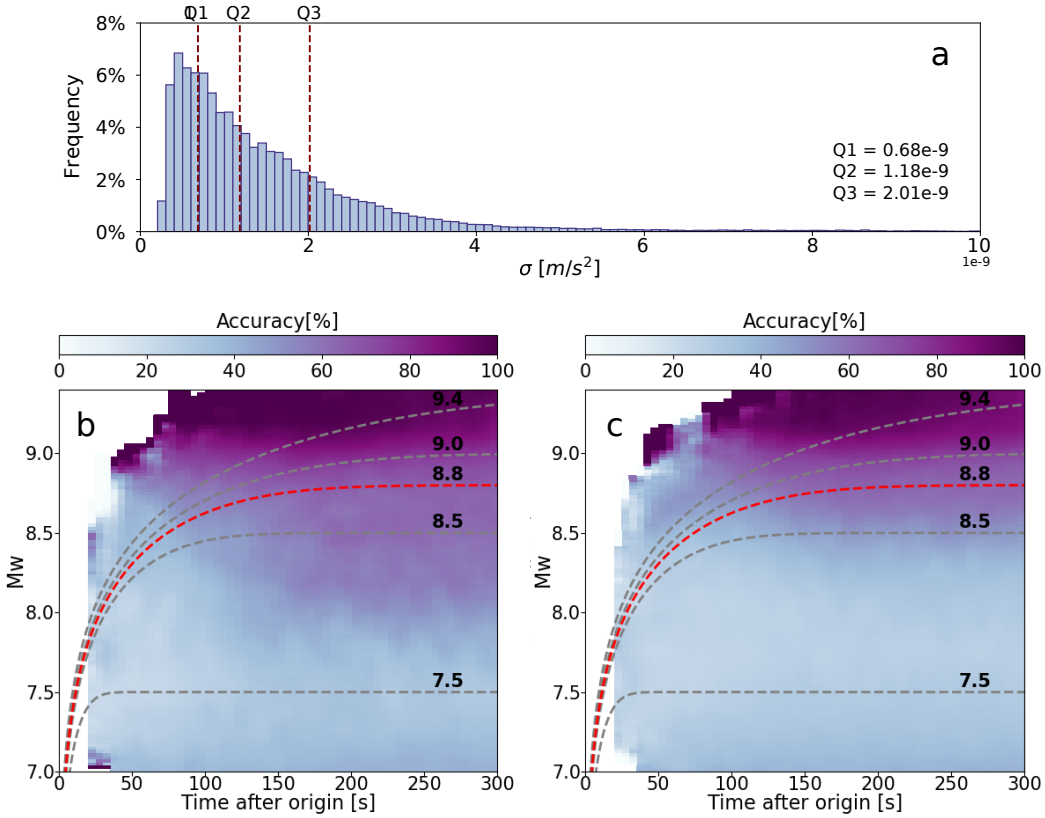

Figure 11. **a** Frequency distribution of the median standard deviation of the noise (σ) for the 2010 network test set, using a 5-min window previous to the event. The dashed red lines indicate the first (Q1), second (Q2) and third (Q3) quartiles. The bottom panels show the accuracy maps computed using the samples of the test set for which (**b**) $\sigma < Q1$ and (**c**) $\sigma > Q3$.

6.2 Test on noiseless data

To explore the theoretical limits of PEGSNet and find an upper limit in the performance, we train and test the model considering an idealized scenario of noiseless data. We use the synthetic PEGS database described previously, but do not add noise. The density plot of the residuals in Figure 14 shows again the evident difference in the time-

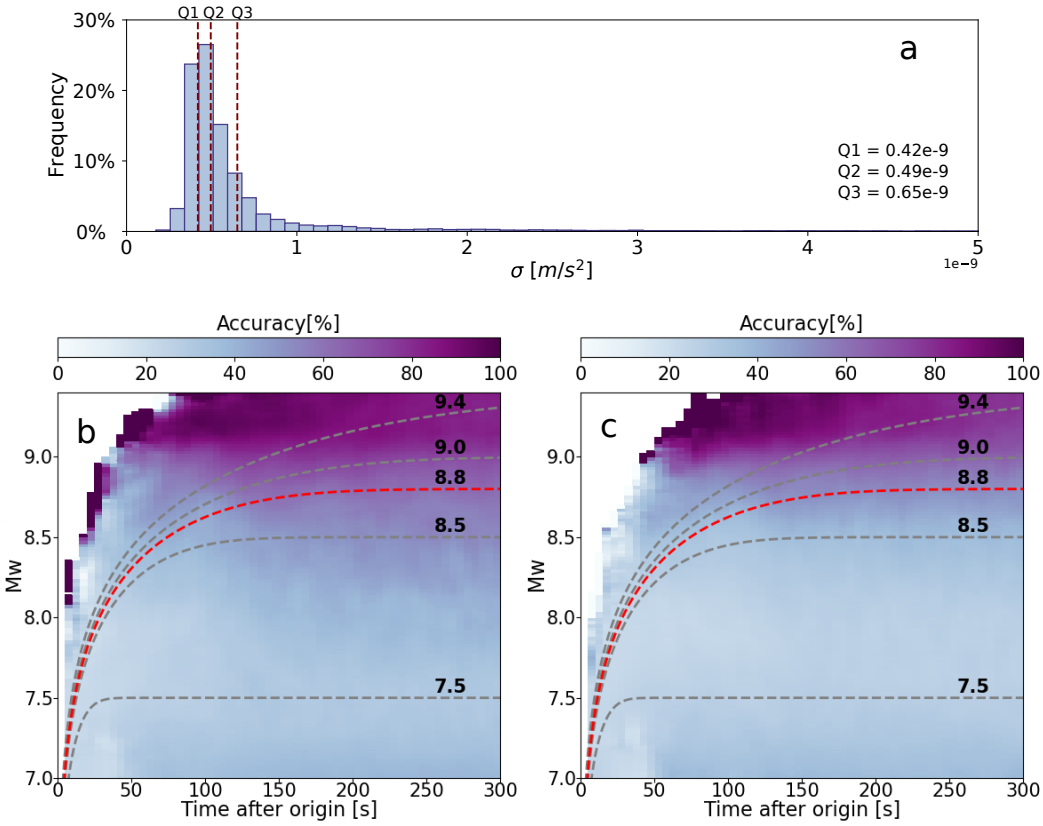

Figure 12. Same as Fig. 11 for the 2021 network.

	2010 network		2021 network	
σ	Accuracy	Misfit	Accuracy	Misfit
$< Q1$	62 %	0.35	59 %	0.39
$> Q3$	59 %	0.43	51 %	0.59

Table 1. Accuracy and misfit values calculated using the $M_w \geq 8.8$ earthquakes 100 s after the origin time and that belong to the first and fourth subset of the test set, for the 2010 and 2021 networks. The first subset (lowest level of noise) contains the samples for which $\sigma < Q1$. The fourth subset (higher level of noise) contains the samples for which $\sigma > Q3$. Q1 and Q3 values are indicated in panel **a** of Figures 11 and 12.

liness of the estimations between the two networks: the 2021 network provides earlier estimates than the 2010 network. The estimations based on the 2010 network start at around 20 s and have errors of ±0.2 after the first 50 s (Fig. 14 **a**). The estimations based on the 2021 network start within 10 s after origin time and have errors of ±0.2 but with higher dispersion up to around 60 s. According to the corresponding accuracy maps (Fig. 13), the first estimates start earlier with the 2021 network but the accuracy is also poorer than with the 2010 network, as discussed in sections 4 and 5.

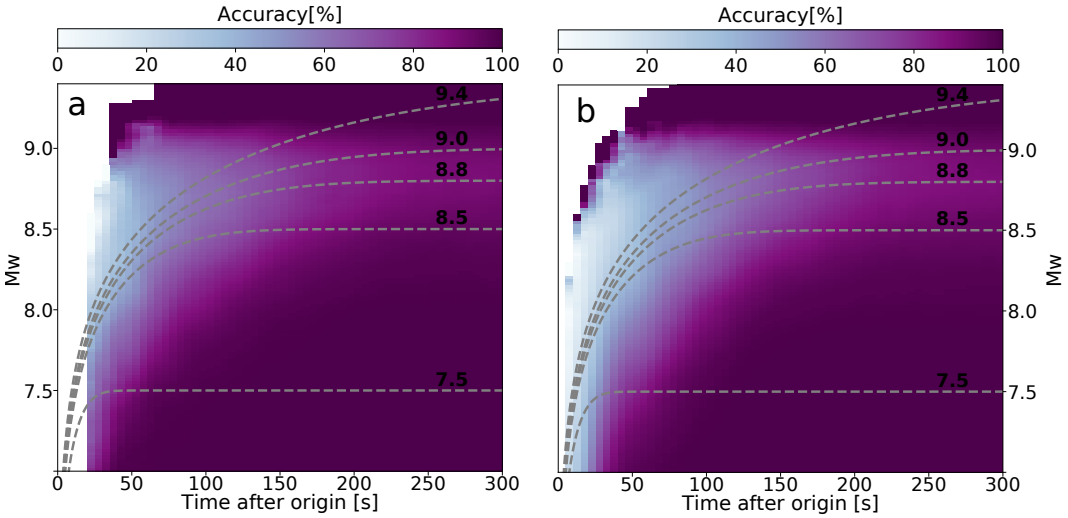

Figure 13. Accuracy map using the noise-free PEGS database, test set only. **a** and **b** correspond to 2010 and 2021 networks, respectively.

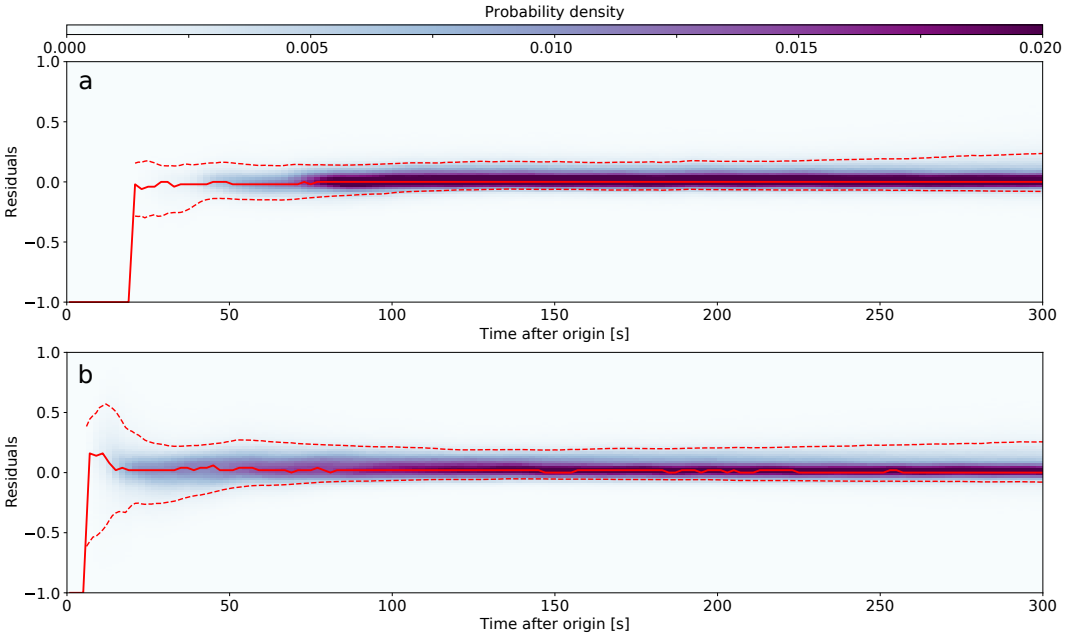

Figure 14. Density plot of the residuals between the predicted magnitude and the ground truth as a function of time for the test set of the noise-free PEGS database. Panels **a** and **b** correspond to the results using the 2010 and 2021 networks, respectively.

7 Conclusion

We trained PEGSNet, a Convolutional Neural Network that estimates the evolution of an earthquake's source time function based on Prompt Elasto-Gravity Signals, with data recorded by the seismic networks available in Chile in 2010 and 2021. The former contains fewer stations and noisier data. Our study confirms that PEGS can be used for rapid estimation of the magnitude of large earthquakes, with performance competitive with GNSS-based algorithms for the 2010 M_w 8.8 Maule earthquake, but without requiring a priori assumptions on slip distribution. The model shows delayed estimations of moment release, but higher accuracy values when using the 2010 configuration. The 2021 network provides accurate estimations sooner owing to its higher number of stations and their proximity to the subduction sources. Nevertheless, this latter aspect played an adverse role in the model performance because the closer stations do not record the PEGS with the largest amplitudes, meaning that PEGSNet is more sensitive to the geometry of the network than to the number of stations. These aspects give us a better outlook on the requirements for improving the performance of PEGS-based early warning approaches, such as the deployment of seismic stations where the larger amplitudes of PEGS are expected, in particular in Argentina.

8 Open Research

8.1 Data Availability Statement

The facilities of IRIS Data Services were used for access to waveform and metadata from IRISDMC (network code: C, C1, G, GT, IU, XH and YS) and GEOFON (network code GE) datacenters. PEGSNet, the CNN used in this work was developed by Licciardi et al. (2022). Figures were made with Matplotlib version 3.3.4

Acknowledgments

This work has received funding from the European Research Council (ERC) under the European Union's Horizon 2020 research and innovation program (Grant Agreement 949221). This work was granted access to the HPC resources of IDRIS under the allocations 2020-AD011012142, 2021-AP011012536 and 2021-A0101012314 made by GENCI. This work has been supported by the French government, through the UCAJEDI Investments in the Future project managed by the National Research Agency (ANR) ANR-15-IDEX-01. BRL acknowledges funding from the JSPS LEADER program and from NASA NSPIRES grant 80NSSC22K1282.

References

Allen, R. M., & Kanamori, H. (2003). The potential for earthquake early warning in southern california. *Science*, *300*, 786-789. doi: 10.1126/science.1080912

Allen, R. M., & Melgar, D. (2019). Earthquake early warning: Advances, scientific challenges, and societal needs. *Annual Review of Earth and Planetary Sciences*, *47*, 361–388.

Bock, Y., & Melgar, D. (2016). Physical applications of pgs geodesy: a review. *Reports on Progress in Physics*, *79*(10). doi: 10.1088/0034-4885/79/10/106801

Boore, D., & Bommer, J. (2005). Processing of strong-motion accelerograms: needs, options and consequences. *Soil Dynamics and Earthquake Engineering*, *25*, 93-115. doi: 10.1016/j.soildyn.2004.10.007

Harms, J. (2016). Transient gravity perturbations from a double-couple in a homogeneous half-space. *Geophysical Journal International*, *205*(2), 1153–1164.

Harms, J., Ampuero, J.-P., Barsuglia, M., Chassande-Mottin, E., Montagner, J.-P., Somala, S., & Whiting, B. (2015). Transient gravity perturbations induced by earthquake rupture. *Geophysical Journal International*, *201*(3), 1416–1425.

Hayes, G., Moore, G., Portner, D., Hearne, M., Flamme, H., Furtney, M., & Smoczyk, G. (2018). Slab2, a comprehensive subduction zone geometry model. *Science*, *362*, 58-61.

Heaton, T. H. (2017). Correspondence: Response of a gravimeter to an instantaneous step in gravity. *Nature Communications*, *8*(1), 1–3.

Hoshiba, M., Iwakiri, K., Hayashimoto, N., Shimoyama, T., Hirano, K., Yamada, Y., ... Kikuta, H. (2011). Outline of the 2011 off the pacific coast of tohoku earthquake (m_w 9.0) — earthquake early warning and observed seismic intensity. *Earth, Planets and Space*, *63*, 547-551.

Hoshiba, M., & Ozaki, T. (2014). Earthquake early warning and tsunami warning of the japan meteorological agency, and their performance in the 2011 off the pacific coast of tohoku earthquake (m_w9.0). In F. Wenzel & J. Zschau (Eds.), *Early warning for geological disasters: Scientific methods and current practice* (pp. 1–28). Berlin, Heidelberg: Springer Berlin Heidelberg. doi: 10.1007/978-3-642-12233-0_1

Juhel, K., Ampuero, J.-P., Barsuglia, M., Bernard, P., Chassande-Mottin, E., Fiorucci, D., ... Whiting, B. (2018). Earthquake early warning using future generation gravity strainmeters. *Journal of Geophysical Research: Solid Earth*, *123*(12), 10–889.

Juhel, K., Montagner, J.-P., Vallée, M., Ampuero, J.-P., Barsuglia, M., Bernard, P., ... Whiting, B. F. (2019). Normal mode simulation of prompt elastogravity signals induced by an earthquake rupture. *Geophysical Journal International*, *216*, 935–947.

Licciardi, A., Bletery, Q., Rouet-Leduc, B., Ampuero, J.-P., & Juhel, K. (2022). Instantaneous tracking of earthquake growth with elastogravity signals. *Nature*, *606*, 319-324.

Lin, J.-T., Melgar, D., Thomas, A., & Searcy, J. (2021). Early warning for great earthquakes from characterization of crustal deformation patterns with deep learning. *Journal of Geophysical Research: Solid Earth*, *126*(10), e2021JB022703.

McGuire, J., Minson, S., Murray, J., & Brooks, B. (2021). The role of geodetic algorithms for earthquake early warning in cascadia. *Geophysical Research Letters*, *48*. doi: 10.1029/2020GL092324

Meier, M.-A., Ampuero, J. P., & Heaton, T. H. (2017). The hidden simplicity of subduction megathrust earthquakes. *Science*, *357*, 1277-1281.

Meier, M.-A., Heaton, T., & Clinton, J. (2016). Evidence for universal earthquake rupture initiation behavior. *Geophysical Research Letters*, *43*, 7991-7996. doi: 10.1002/2016GL070081

Melgar, D., Allen, R. M., Riquelme, S., Geng, J., Bravo, F., Baez, J. C., ... Smalley, R. J. (2016). Local tsunami warnings: Perspectives from recent large events. *Geophysical Research Letters*, *43*, 1109-1117. doi: 10.1002/2015GL067100

Melgar, D., & Bock, Y. (2013). Near-field tsunami models with rapid earthquake source inversions from land- and ocean-based observations: The potential for forecast and warning. *Journal of Geophysical Research: Solid Earth*, *118*, 5939-5955. doi: 10.1002/2013JB010506

Minson, S. E., Meier, M.-A., Baltay, A. S., Hanks, T. C., & Cochran, E. S. (2018). The limits of earthquake early warning: Timeliness of ground motion estimates. *Science advances*, *4*(3), eaaq0504.

Minson, S. E., Murray, J. R., Langbein, J. O., & Gomberg, J. S. (2014). Real-time inversions for finite fault slip models and rupture geometry based on high-rate gps data. *Journal of Geophysical Research: Solid Earth*, *119*(4), 3201–3231.

Montagner, J.-P., Juhel, K., Barsuglia, M., Ampuero, J. P., Chassande-Mottin, E., Harms, J., ... Lognonné, P. (2016). Prompt gravity signal induced by the 2011 tohoku-oki earthquake. *Nature communications*, *7*(1), 1–7.

Ruhl, C., Melgar, D., Grapenthin, R., & Allen, R. M. (2017). The value of real-time

gnss to earthquake early warning. *Geophysical Research Letters*, *44*, 8311-8319. doi: 10.1002/2017GL074502

Ruhl, C. J., Melgar, D., Chung, A. I., Grapenthin, R., & Allen, R. M. (2019). Quantifying the value of real-time geodetic constraints for earthquake early warning global seismic and geodetic data set. *Journal of Geophysical Research: Solid Earth*, *124*, 3819-3837.

Setiyono, U., Gusman, A. R., Satake, K., & Fujii, Y. (2017). Pre-computed tsunami inundation database and forecast simulation in pelabuhan ratu, indonesia. *Pure and Applied Geophysics*, *174*, 3219–3235. doi: 10.1007/s00024-017-1633-8

Shimoda, T., Juhel, K., Ampuero, J.-P., Montagner, J.-P., & Barsuglia, M. (2021). Early earthquake detection capabilities of different types of future-generation gravity gradiometers. *Geophysical Journal International*, *224*(1), 533–542.

Vallée, M., Ampuero, J.-P., Juhel, K., Bernard, P., Montagner, J.-P., & Barsuglia, M. (2017). Observations and modeling of the elastogravity signals preceding direct seismic waves. *Science*, *358*, 1164-1168.

Vallée, M., & Douet, V. (2016). A new database of source time functions (STFs) extracted from the SCARDEC method. *Physics of the Earth and Planetary Interiors*, *257*, 149-157.

Vallée, M., & Juhel, K. (2019). Multiple observations of the prompt elastogravity signals heralding direct seismic waves. *Journal of Geophysical Research: Solid Earth*, *124*, 2970-2989.

Wu, Y.-M., & Zhao, L. (2006). Magnitude estimation using the first three seconds p-wave amplitude in earthquake early warning. *Geophysical Research Letters*, *33*, L16312. doi: 10.1029/2006GL026871

Zhang, S., Wang, R., & Chen, X. (2022). Seismic prompt gravity strain signals in a layered spherical earth. *Available at SSRN 4245177*. doi: https://ssrn.com/abstract=4245177

Zhang, S., Wang, R., Dahm, T., Zhou, S., & Heimann, S. (2020). Prompt elastogravity signals (pegs) and their potential use in modern seismology. *Earth and Planetary Science Letters*, *536*, 116150.

Figure1.

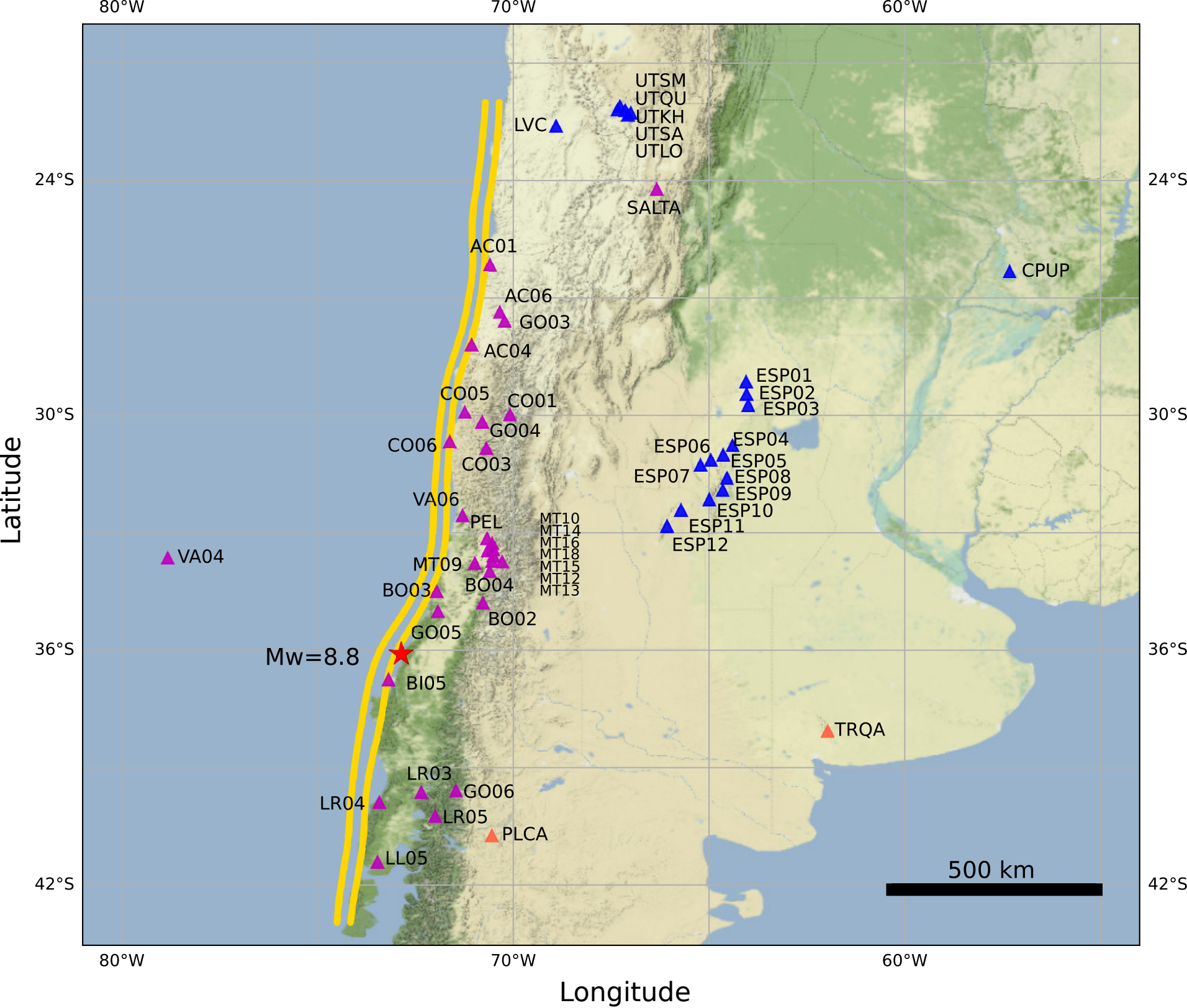
80°W
70°W
60°W
24°S
30°S
36°S
42°S
Latitude
Longitude
UTSM
UTQU
UTKH
UTSA
UTLO
LVC
SALTA
CPUP
AC01
AC06
GO03
AC04
CO05
CO01
GO04
CO06
CO03
VA06
PEL
MT10
MT14
MT16
MT18
MT15
MT12
MT13
MT09
BO04
BO03
BO02
GO05
Mw=8.8
BI05
VA04
ESP01
ESP02
ESP03
ESP04
ESP06
ESP05
ESP07
ESP08
ESP09
ESP10
ESP11
ESP12
TRQA
LR03
GO06
LR04
LR05
PLCA
LL05
500 km

Figure2.

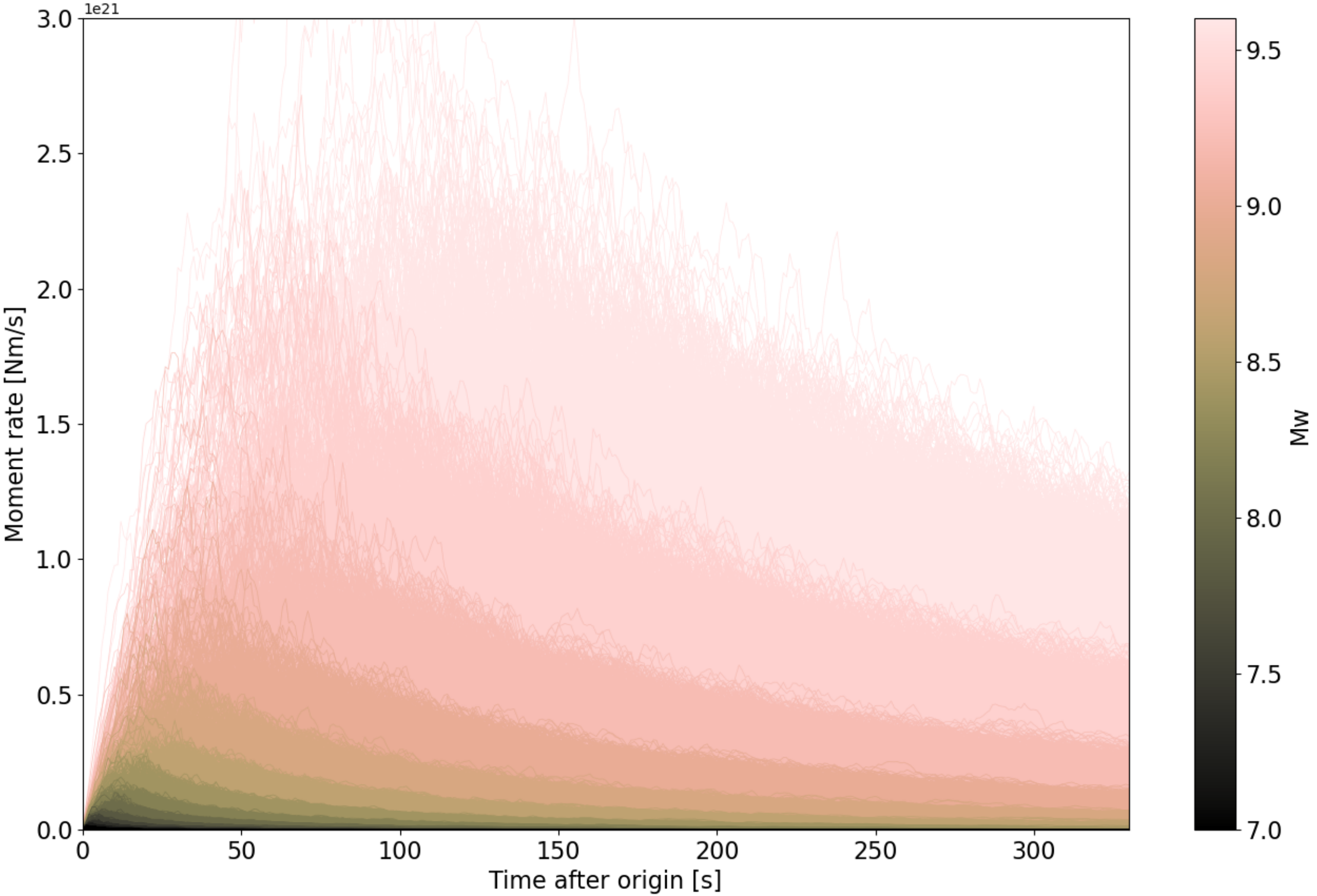
1e21
3.0
2.5
2.0
1.5
1.0
0.5
0.0
Moment rate [Nm/s]
0
50
100
150
200
250
300
Time after origin [s]
9.5
9.0
8.5
8.0
7.5
7.0
Mw

Figure3.

a

Convolutional layer
ReLu activation
Maxpooling layer
Spatial dropout layer
Dense layer

M
N
N
M
M/2
N/2
M/4
N/4
M/8
N/8
32 Cv1
32 Cv2
32 Cv3
32 Cv4
64 Conv5
64 Conv6
128 Conv7
Dense1
512
Dense2
256
Output
3

b

T_1
T_2
Station ID
Time after origin [s]
Scaled amplitude

c

M_w label
M_w
M_w (T_2)
Time after origin [s]

Figure4.

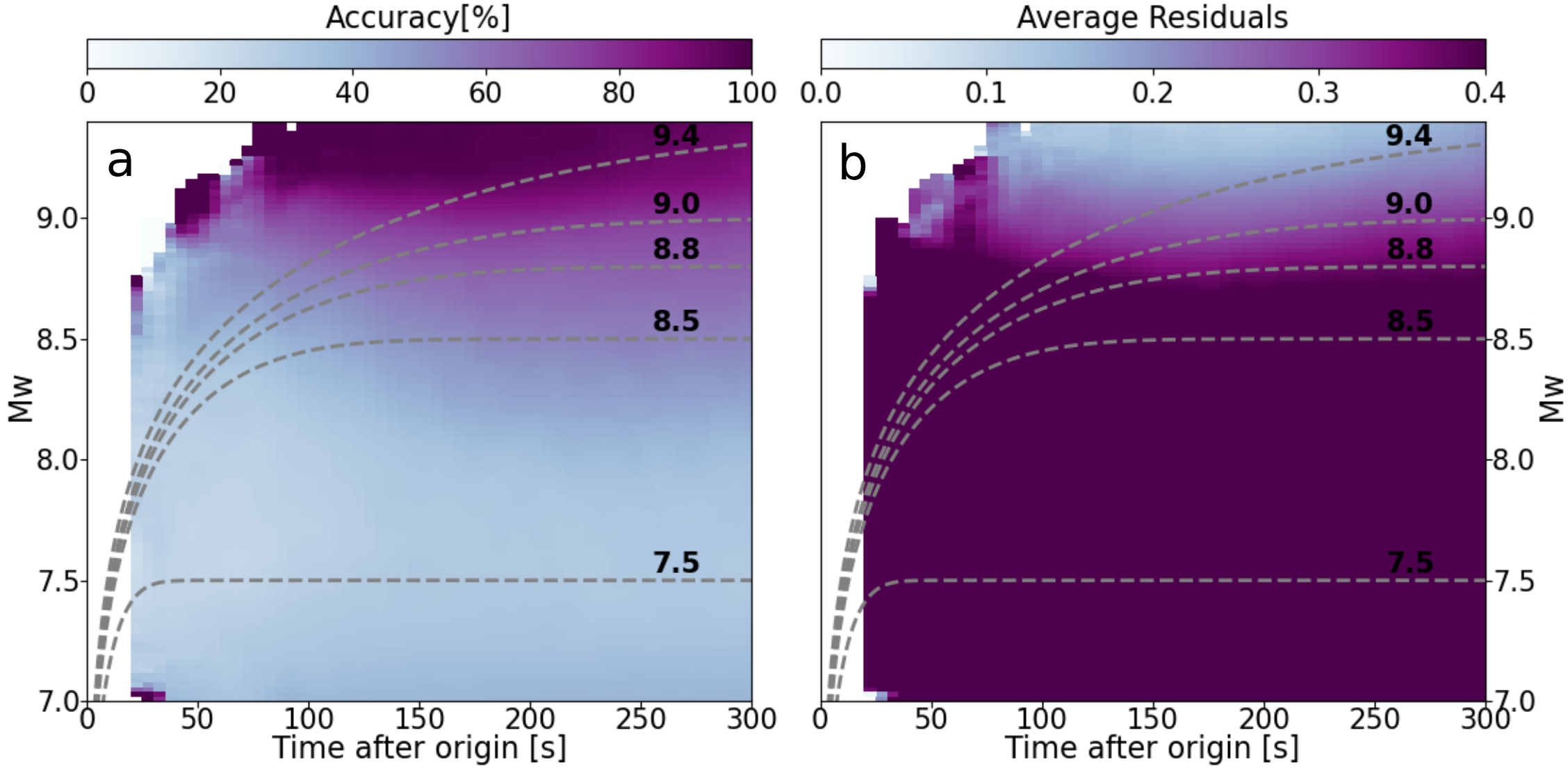
Accuracy[%]
0
20
40
60
80
100
Average Residuals
0.0
0.1
0.2
0.3
0.4
a
b
9.4
9.0
8.8
8.5
7.5
Mw
9.0
8.5
8.0
7.5
7.0
0
50
100
150
200
250
300
Time after origin [s]

Figure5.

Probability density

0.000 0.001 0.002 0.003 0.004 0.005

a

b

M_w

9.5 9.0 8.5 8.0 7.5 7.0

0 50 100 150 200 250 300

Time after origin [s]

Figure6.

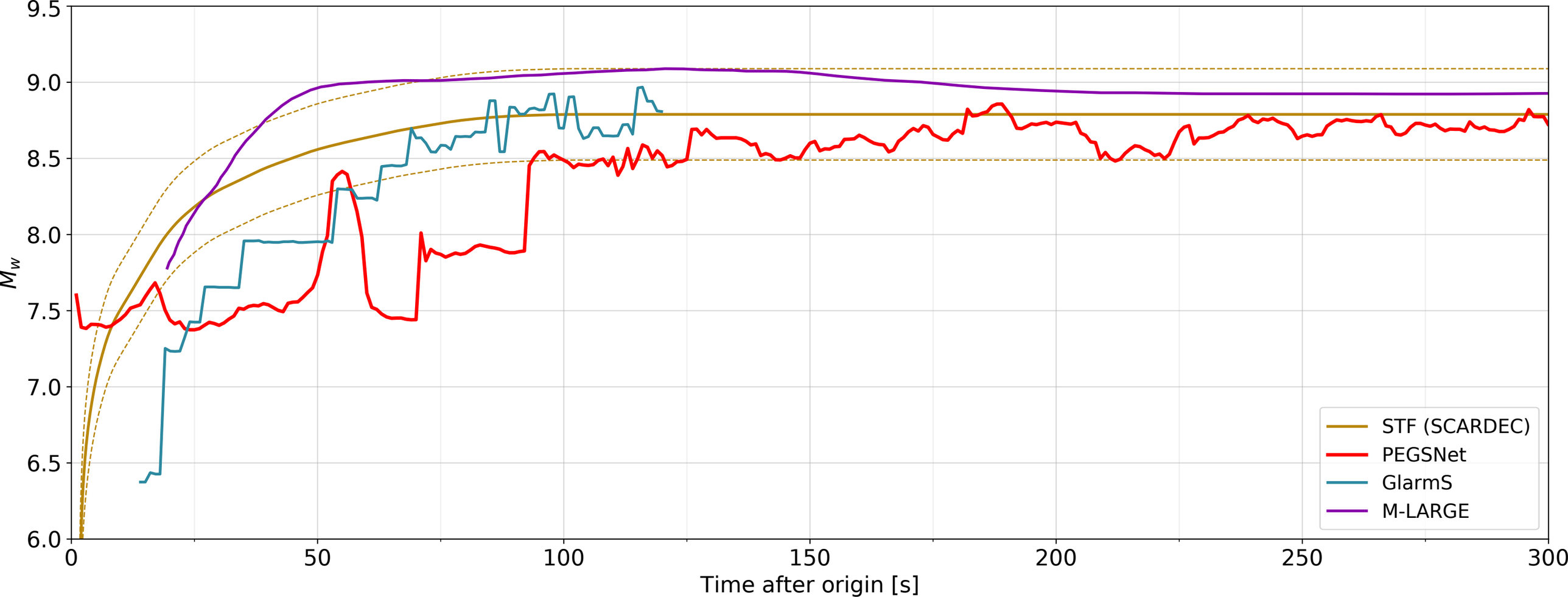
9.5
9.0
8.5
8.0
7.5
7.0
6.5
6.0
M_w
0
50
100
150
200
250
300
Time after origin [s]
STF (SCARDEC)
PEGSNet
GlarmS
M-LARGE

Figure7.

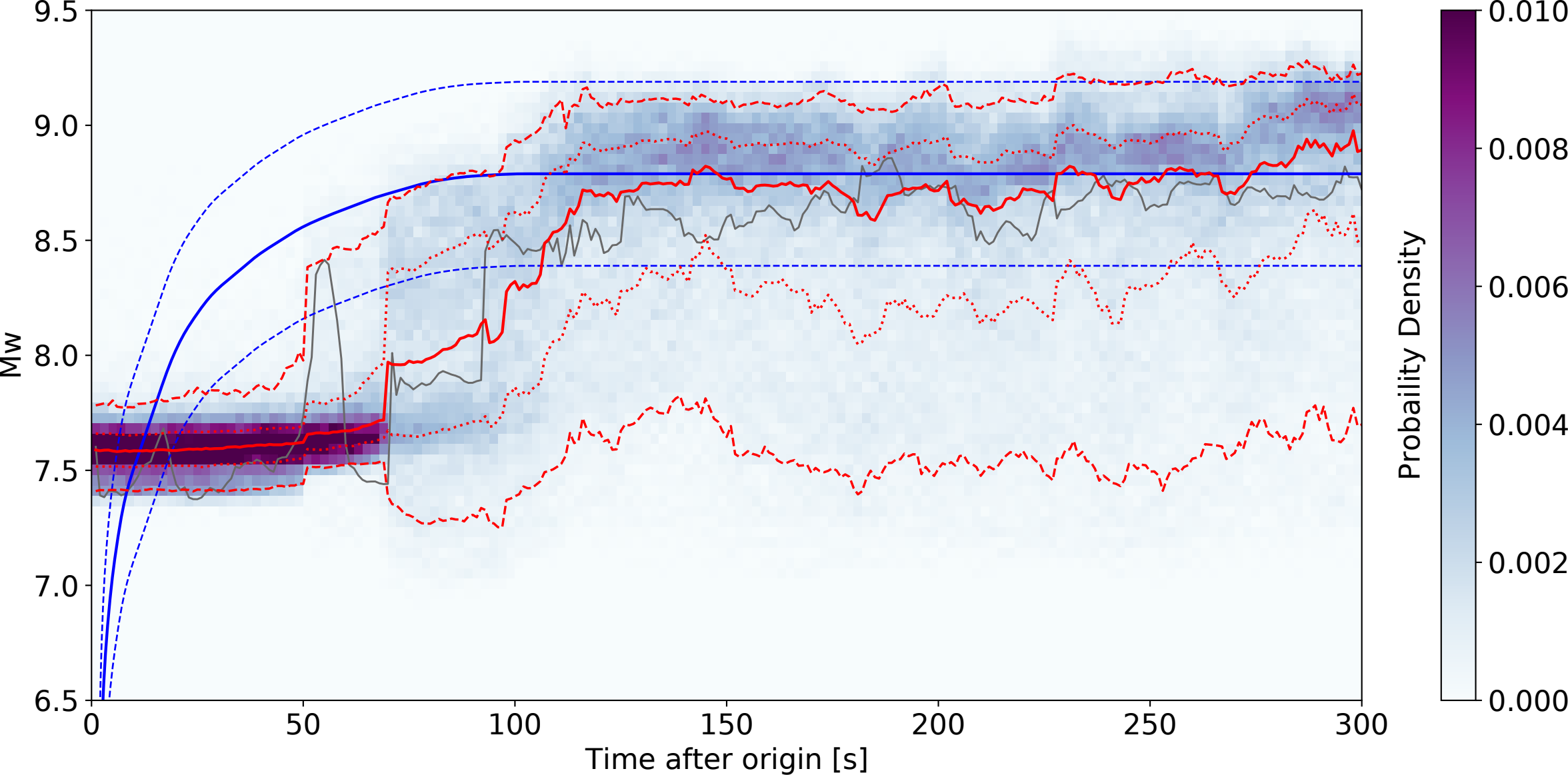
9.5
9.0
8.5
8.0
7.5
7.0
6.5
Mw
0
50
100
150
200
250
300
Time after origin [s]
0.010
0.008
0.006
0.004
0.002
0.000
Probaility Density

Figure8.

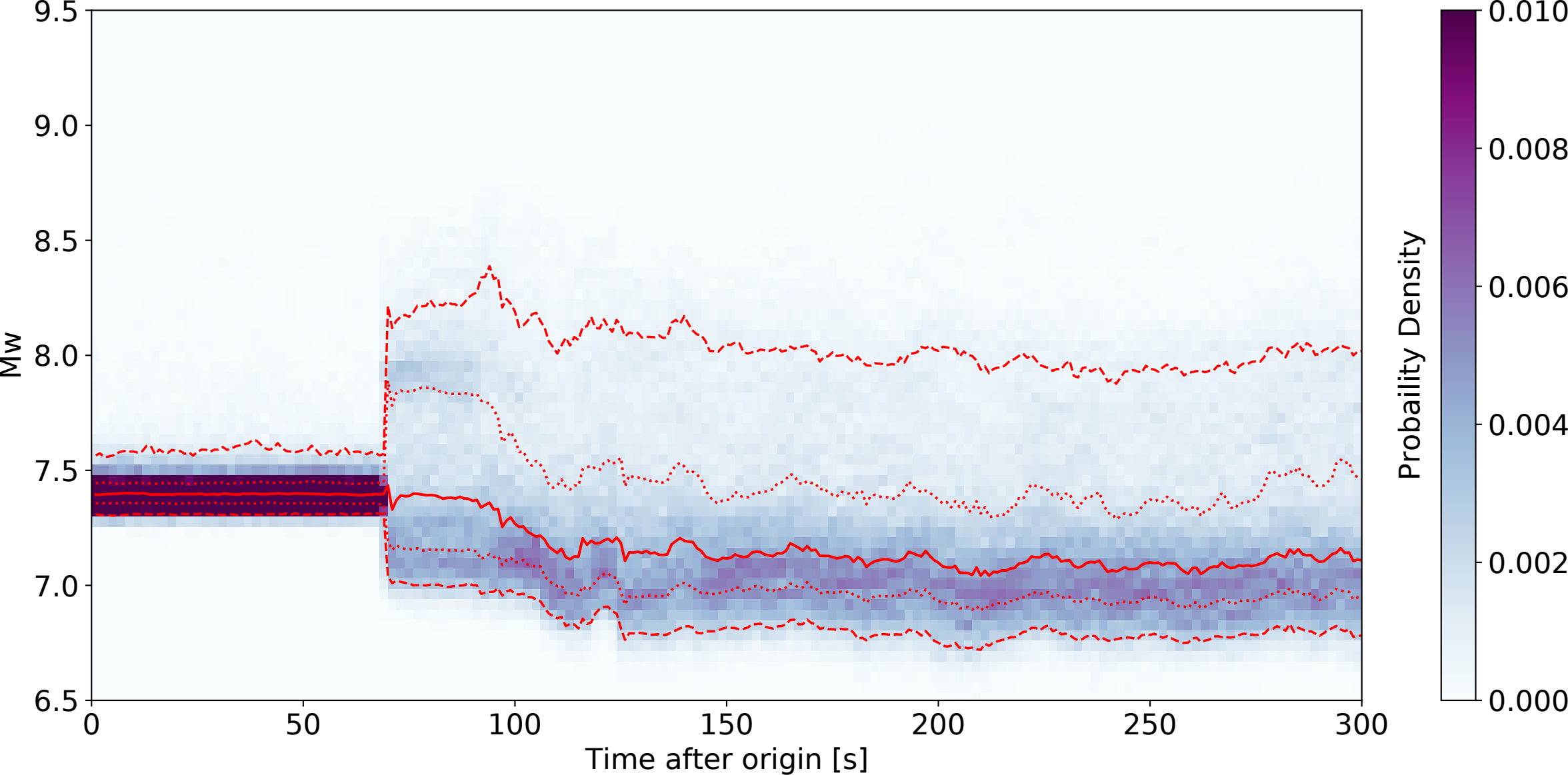
9.5
9.0
8.5
8.0
7.5
7.0
6.5
Mw
0
50
100
150
200
250
300
Time after origin [s]
0.010
0.008
0.006
0.004
0.002
0.000
Probaility Density

Figure9.

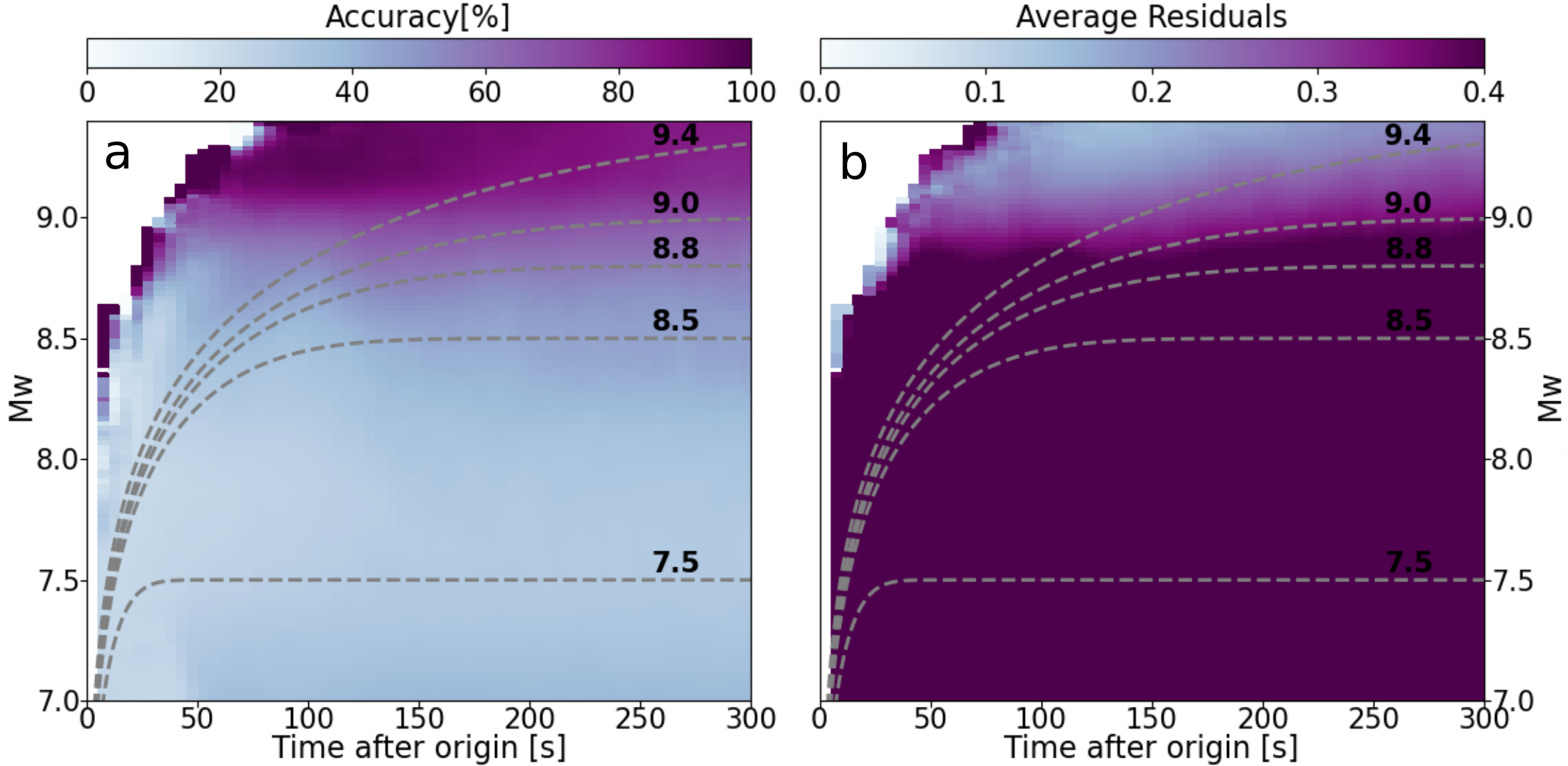
Accuracy[%]
0
20
40
60
80
100
Average Residuals
0.0
0.1
0.2
0.3
0.4
a
b
9.4
9.0
8.8
8.5
7.5
Mw
9.0
8.5
8.0
7.5
7.0
0
50
100
150
200
250
300
Time after origin [s]

Figure10.

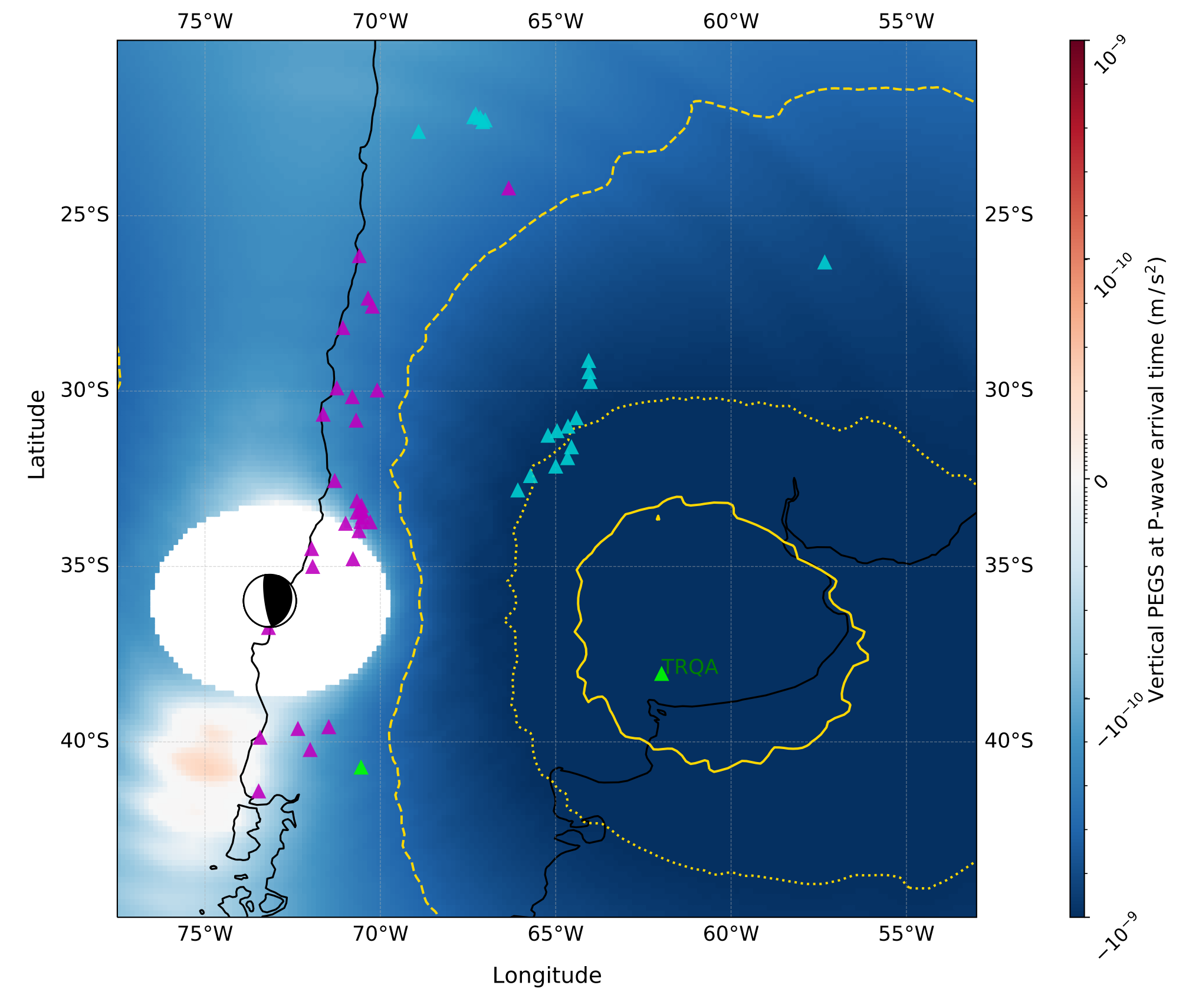
75°W
70°W
65°W
60°W
55°W
25°S
30°S
35°S
40°S
Latitude
Longitude
TRQA
Vertical PEGS at P-wave arrival time (m/s²)
10⁻⁹
10⁻¹⁰
0
−10⁻¹⁰
−10⁻⁹

Figure11.

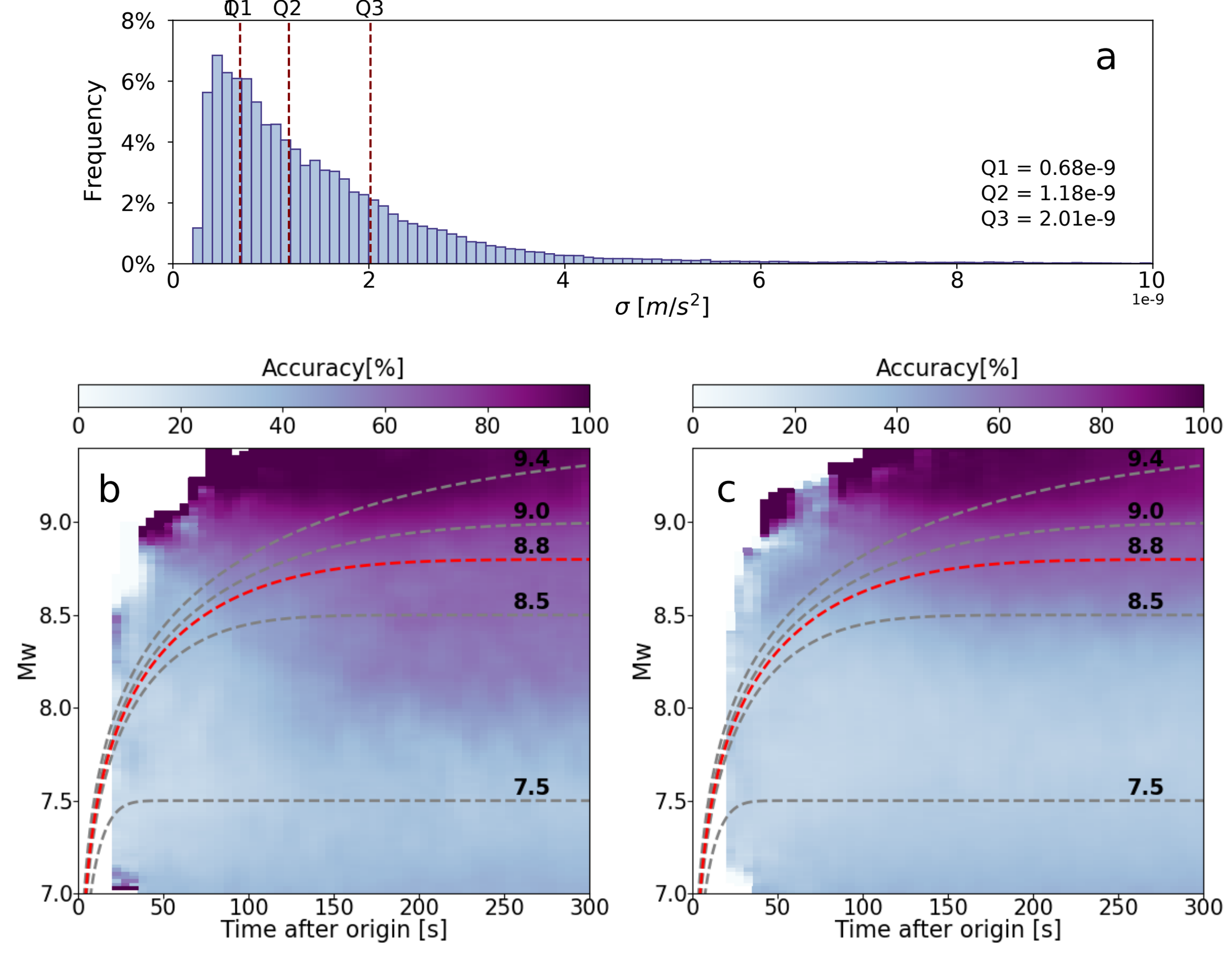
a
Q1
Q2
Q3
Q1 = 0.68e-9
Q2 = 1.18e-9
Q3 = 2.01e-9
Frequency
8%
6%
4%
2%
0%
0
2
4
6
8
10
1e-9
σ [m/s²]
Accuracy[%]
0
20
40
60
80
100
b
c
9.4
9.0
8.8
8.5
7.5
Mw
9.0
8.5
8.0
7.5
7.0
0
50
100
150
200
250
300
Time after origin [s]

Figure12.

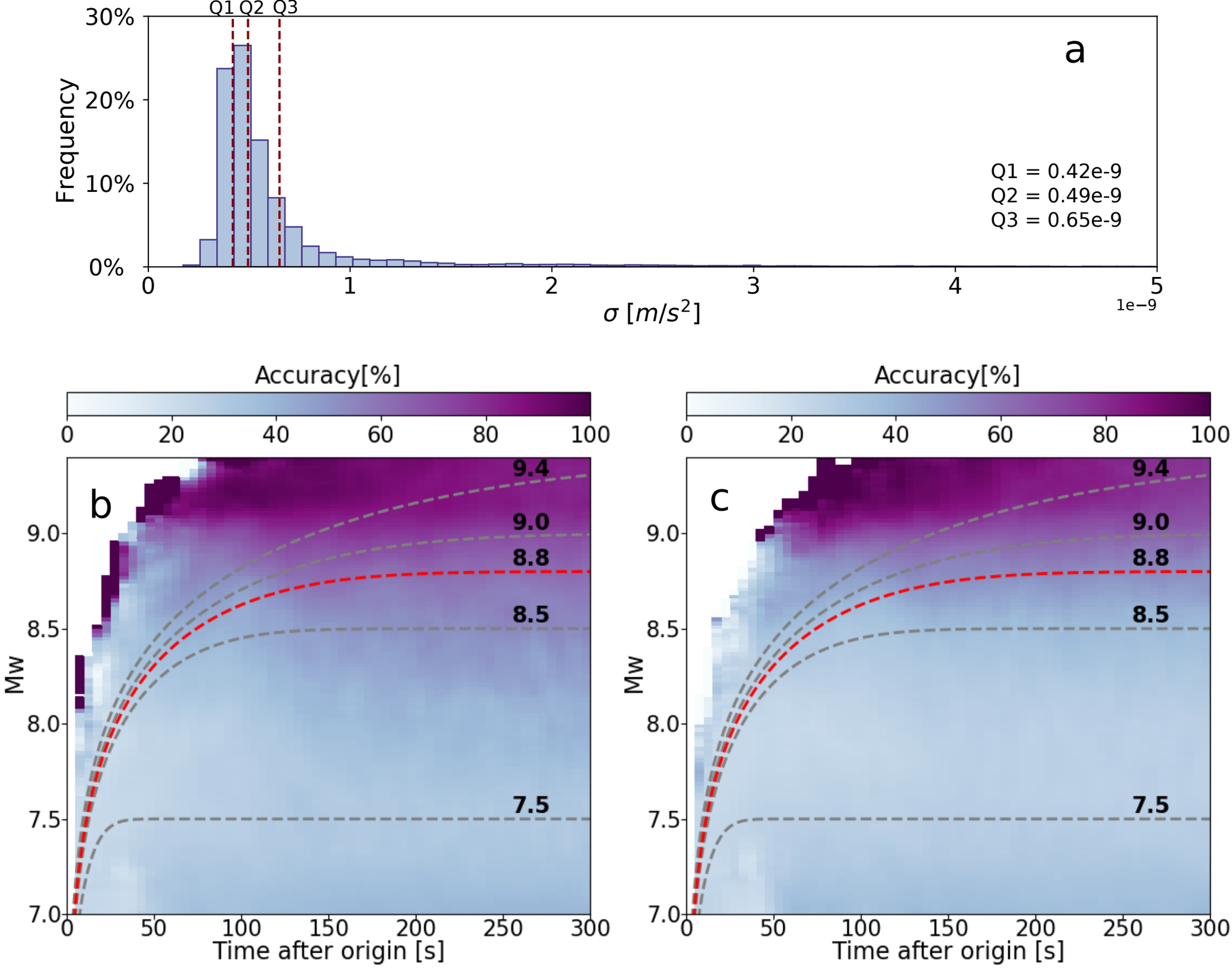
a
Q1 Q2 Q3
30%
20%
10%
0%
Frequency
Q1 = 0.42e-9
Q2 = 0.49e-9
Q3 = 0.65e-9
0
1
2
3
4
5
1e−9
σ [m/s²]
Accuracy[%]
0
20
40
60
80
100
b
c
9.4
9.0
8.8
8.5
7.5
Mw
9.0
8.5
8.0
7.5
7.0
0
50
100
150
200
250
300
Time after origin [s]

Figure13.

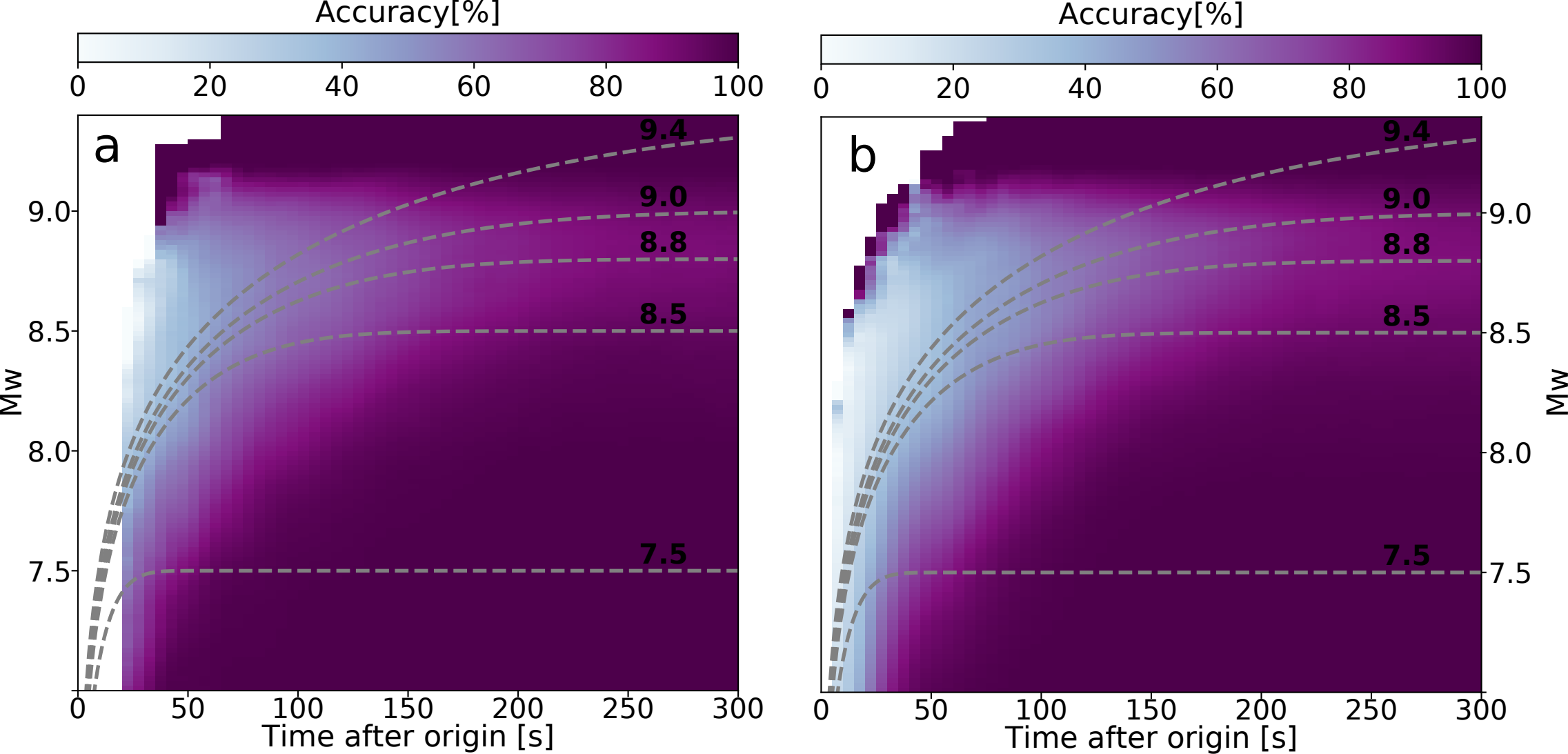
Accuracy[%]
0
20
40
60
80
100
a
b
9.4
9.0
8.8
8.5
7.5
Mw
9.0
8.5
8.0
7.5
0
50
100
150
200
250
300
Time after origin [s]

Figure14.

Probability density

0.000 0.005 0.010 0.015 0.020

a

Residuals

1.0 0.5 0.0 −0.5 −1.0

0 50 100 150 200 250 300

Time after origin [s]

b

Residuals

1.0 0.5 0.0 −0.5 −1.0

0 50 100 150 200 250 300

Time after origin [s]